STRUCTURAL BIOLOGY

Architecture and regulation of an enterobacterial cellulose secretion system

Wiem Abidi[1,2,3]*, Samira Zouhir[1,2,3]*, Meryem Caleechurn[1], Stéphane Roche[1], Petya Violinova Krasteva[1,2,3]†

Many free-living and pathogenic enterobacteria secrete biofilm-promoting cellulose using a multicomponent, envelope-embedded Bcs secretion system under the control of intracellular second messenger c-di-GMP. The molecular understanding of system assembly and cellulose secretion has been largely limited to the crystallographic studies of a distantly homologous BcsAB synthase tandem and a low-resolution reconstruction of an assembled macrocomplex that encompasses most of the inner membrane and cytosolic subunits and features an atypical layered architecture. Here, we present cryo-EM structures of the assembled Bcs macrocomplex, as well as multiple crystallographic snapshots of regulatory Bcs subcomplexes. The structural and functional data uncover the mechanism of asymmetric secretion system assembly and periplasmic crown polymerization and reveal unexpected subunit stoichiometry, multisite c-di-GMP recognition, and ATP-dependent regulation.

INTRODUCTION

Bacterial cellulose is a widespread extracellular matrix component that can modulate microbial fitness and virulence in both environmental settings and infected hosts (*1*–*3*). Whereas its biosynthesis typically involves direct c-di-GMP (cyclic diguanosine monophosphate or CDG) control of an inner membrane (IM) BcsAB synthase duo across the bacterial domain of life, in many β- and γ-proteobacteria it is carried out by sophisticated *Escherichia coli*–like Bcs secretion systems, where multiple accessory subunits are essential for secretion or contribute to the optimal production of the polysaccharide in vivo (*1*, *4*).

In particular, the *E. coli* cellulose secretion machinery comprises a total of nine subunits (BcsRQABZCEFG) that span from the cytosol to the extracellular space (Fig. 1A) (*1*). Studies on a BcsAB complex from *Rhodobacter sphaeroides* have shown that processive glucose polymerization is likely carried out by a glycosyl transferase domain of BcsA, whose active site is made accessible by recurrent binding of dimeric c-di-GMP to an adjacent PilZ domain and displacement of a gating loop capping the substrate-binding pocket (*5*–*7*). IM transport is coupled to processive polymerization and is energized by the high-energy phosphoanhydride bonds of the preactivated synthase substrate, uridine diphosphate (UDP)–glucose. The nascent polysaccharide chain is thus extruded, one molecule at a time, through the IM transport domain of BcsA, completed by the C-terminal tail-anchor of partner BcsB (*8*). In the periplasm, the latter features a donut-shaped architecture and is proposed to lead the outcoming cellulose toward the outer membrane secretory component BcsC (*6*). In addition, the periplasmic modules of BcsG and BcsZ can introduce post-synthetic, covalent modifications in the nascent polysaccharide through the addition of phosphoethanolamine residues or limited hydrolysis, respectively (*1*, *9*). Last, *E. coli*–like cellulose secretion in vivo is absolutely dependent on the presence of two small cytosolic proteins, BcsR and BcsQ, and is substantially enhanced by a third cytosolic protein, BcsE, as well as by a short membrane–embedded polypeptide, BcsF (*4*).

We recently uncovered complex interdependence among these regulatory subunits and showed that most of the IM and cytosolic Bcs components (BcsRQABEF) form a megadalton-sized secretory macrocomplex with a multimeric, layered, and asymmetric architecture (Fig. 1A) (*4*, *10*). Nevertheless, the structures, localization, and functional roles of individual building subunits within the secretory assembly remained largely unresolved. Here, we provide near-atomic resolution cryo–electron microscopy (cryo-EM) data that reveal noncanonical synthase tandem assembly and β-sheet complementation–driven BcsB polymerization in the periplasm that can explain both the unusual secretion system asymmetry and its targeting to cell pole in vivo (*4*, *11*). We further present the crystal structures of several multicomponent regulatory subcomplexes, which suggest additional regulatory inputs via BcsRQ-dependent adenosine triphosphate (ATP) complexation, multisite c-di-GMP recognition, and creation of a synthase-proximal c-di-GMP pool for processive enzyme activation.

RESULTS

Structure, polymerization, and asymmetry of the periplasmic crown

To gain further insights into the architecture of the purified Bcs macrocomplex, we resorted to single-particle cryo-EM (Fig. 1, B and C, and fig. S1). The three-dimensional (3D) electron density reconstruction was characterized by substantial gradient of estimated local resolution, with lower values for the transmembrane and cytosolic regions, likely due to the presence of a detergent micelle, partial complex dissociation, and conformational variability among single particles. In contrast, the periplasmic domains were resolved at nearly atomic resolution (average resolution of 2.9 Å without imposed symmetry; fig. S1), with most of the particles featuring up to six BcsB copies in the crown. As the averaged electron density corresponding to the sixth BcsB protomer presented lower intensity and resolution, a pentameric BcsB assembly was refined against the experimental density (table S1). The data confirm that the crown is composed exclusively of multiple BcsB copies and reveal that the protein polymerizes in a

[1]Institute for Integrative Biology of the Cell (I2BC), CEA, CNRS, Université Paris-Sud, 91198 Gif- sur-Yvette, France. [2]"Structural Biology of Biofilms" Group, European Institute of Chemistry and Biology (IECB), 33600 Pessac, France. [3]CBMN UMR 5248 CNRS, University of Bordeaux, 33600 Pessac, France.
*These authors contributed equally to this work.
†Corresponding author. Email: pv.krasteva@iecb.u-bordeaux.fr

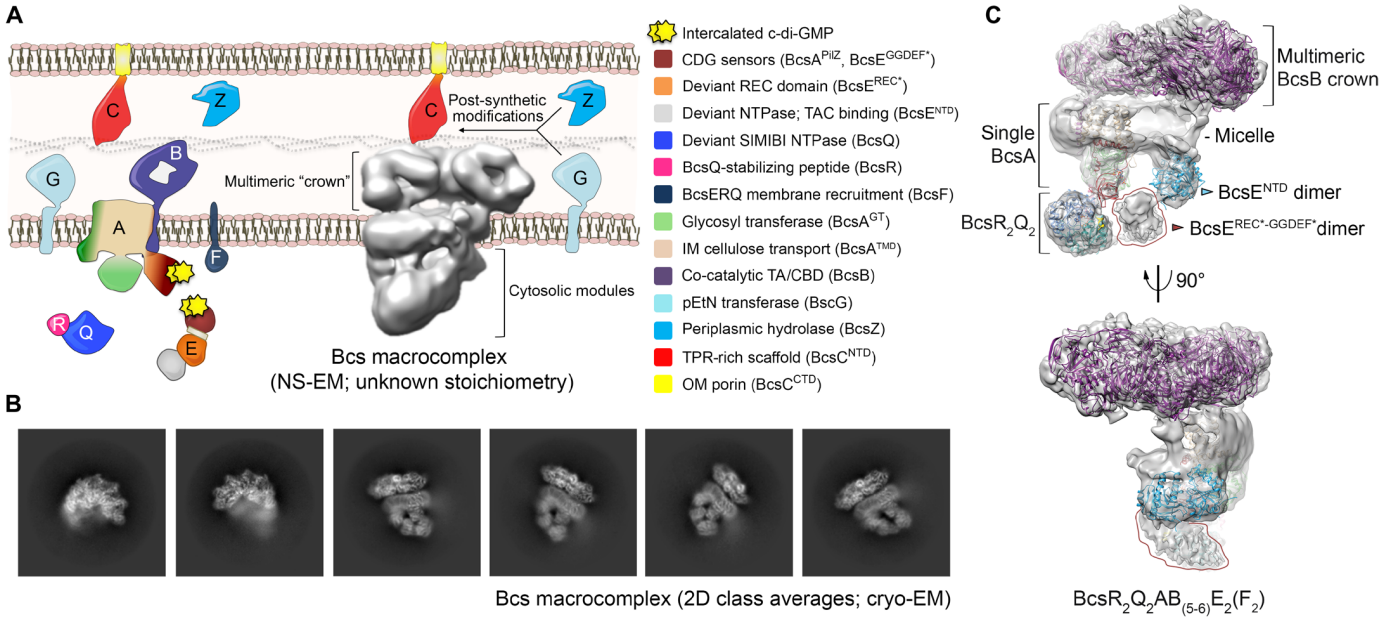

Fig. 1. The *E. coli*–like cellulose secretion system and architecture of the Bcs macrocomplex. (**A**) Left: Topology and functional roles of Bcs subunits (NS-EM, negative-stain electron microscopy; CDG, c-di-GMP; REC, receiver; NTPase, nucleoside triphosphatase; TAC, transcription antitermination complex; NTD, N-terminal domain; SIMIBI, signal recognition particle, MinD, and BioD; IM, inner membrane; TMD, transmembrane domain; TA, tail-anchor; CBD, carbohydrate-binding domains; pEtN, phosphoethanolamine; TPR, tetratricopeptide repeats; OM, outer membrane; CTD, C-terminal domain). Right: Structure of an assembled Bcs macrocomplex encompassing most IM and cytosolic subunits as obtained by single-particle NS-EM (*1*). (**B**) Cryo-EM 2D class averages of detergent-extracted and affinity-purified Bcs macrocomplex. (**C**) Density assignments within the assembled Bcs macrocomplex. A hexameric BcsB crown derived from the locally refined $BcsB^{peri}$ pentamer (see below) was fitted in the periplasmic densities. A model of a CDG-bound BcsA was generated by homology modeling in Robetta and was then fitted and refined against the densities corresponding to the BcsRQAB subcomplex, themselves improved by local refinement. The crystal structure of a sandwich $BcsR_2Q_2$ dimer was fitted in the apical densities, with BcsR adopting an extended four-turn α1 helix, as observed in some of the crystallized states (see below). A Robetta-derived model of dimeric $BcsE^{NTD}$ was fitted in the membrane-proximal densities opposite BcsA. The $BcsE^{NTD}$ copies are fitted in head-to-tail orientation consistent with recently reported interaction data (*10*). Regions corresponding to $BcsE^{Rec*\text{-}GGDEF*}$ did not yield interpretable densities even after local refinement, likely due to conformational heterogeneity (see below). Most BcsB tail-anchors as well as the BcsE-interacting BcsF chains (predicted to fold into a single transmembrane helix each) were not visible in the 3D-reconstructed micelle.

helical fashion to introduce asymmetry to the system rather than axial symmetry that is typical for multicopy secretion system assemblies (fig. S1) (*12*).

Each BcsB subunit adopts a conserved four-domain fold (D1 to D4) in the periplasm ($BcsB^{peri}$) composed of two CBD jellyrolls and two flavodoxin-like domains, alternating from the N-terminus toward a C-proximal amphipathic helix and an IM tail-anchor (TA) (Fig. 2A and fig. S2). The latter is visible and well refined only in the membrane-proximal BcsB protomer interacting with the BcsA synthase (see below); however, the lack of biochemically detectable BcsB cleavage and the presence of a large detergent micelle underneath the entire crown indicate that all crown BcsB subunits likely feature preserved IM tails. Although the sequence identity with the *R. sphaeroides* homolog is overall low, the four domains adopt similar secondary and tertiary structures with several crucial exceptions (Fig. 2A and fig. S2, A and B). First, D2 of $BcsB^{E.coli}$ features a C-proximal β-strand insertion (*E. coli* residues S^{343}-P^{351}) that extends the central β-sheet of the domain, whereas D4 lacks an amphipathic helix found in the region connecting strands β2 and β3 of the domain's central β-sheet in the $BcsB^{R.sphaeroides}$ homolog (*R. sphaeroides* residues W^{570}-R^{594}). In contrast, surrounding D4 residues in the *E. coli* protein adopt a three-stranded β-sheet fold, which is complemented by the D2 β-strand insertion of the neighboring subunit to form a continuous nine-stranded shared β-sheet and provide a secondary structure-dependent mechanism for periplasmic BcsB polymerization that is likely conserved among enterobacteria (Fig. 2, A and B, and fig. S2). Second, D3 of $BcsB^{E.coli}$ features an extended β-strand hairpin in one of the β-sheet–connecting loops in the jellyroll. Within the macrocomplex, D3 hairpins point toward the center of the BcsB crown, where they are further stabilized by intersubunit β-strand contacts and pack tightly in a helical staircase-like fashion (figs. S1 and S2). In the *R. sphaeroides* BcsAB crystal structures, the newly synthesized cellulose exiting BcsA's IM transport domain positions along the membrane-proximal surface of BcsB's D3 module (Fig. 2A). Structural superposition with the cryo-EM structure presented here indicates that in *E. coli* the secreted cellulose is likely extruded toward the BcsB crown lumen and away from the peripheral D2 and D4 flavodoxin-like domains. Together, these data suggest that D2 and D4 play a role in interactions with the periplasmic peptidoglycan rather than the secreted polysaccharide, whereas the stacked D3 luminal loops might provide a ratchet-like structural support for the secreted homopolymer on its way toward the outer membrane.

A modeled $BcsB^{peri}$ superhelix features about nine protomers per turn, with the 10th BcsB copy showing a 91-Å vertical displacement relative to the first or almost twice the IM thickness (fig. S1D). Given that BcsB is a tail-anchored protein, its helical polymerization would induce substantial deformation of the IM, which by itself is likely to act as a polymerization-limiting factor. Non-aggregative cross-linking analyses (fig. S1, E and F) (*13*) and the cryo-EM structure of purified,

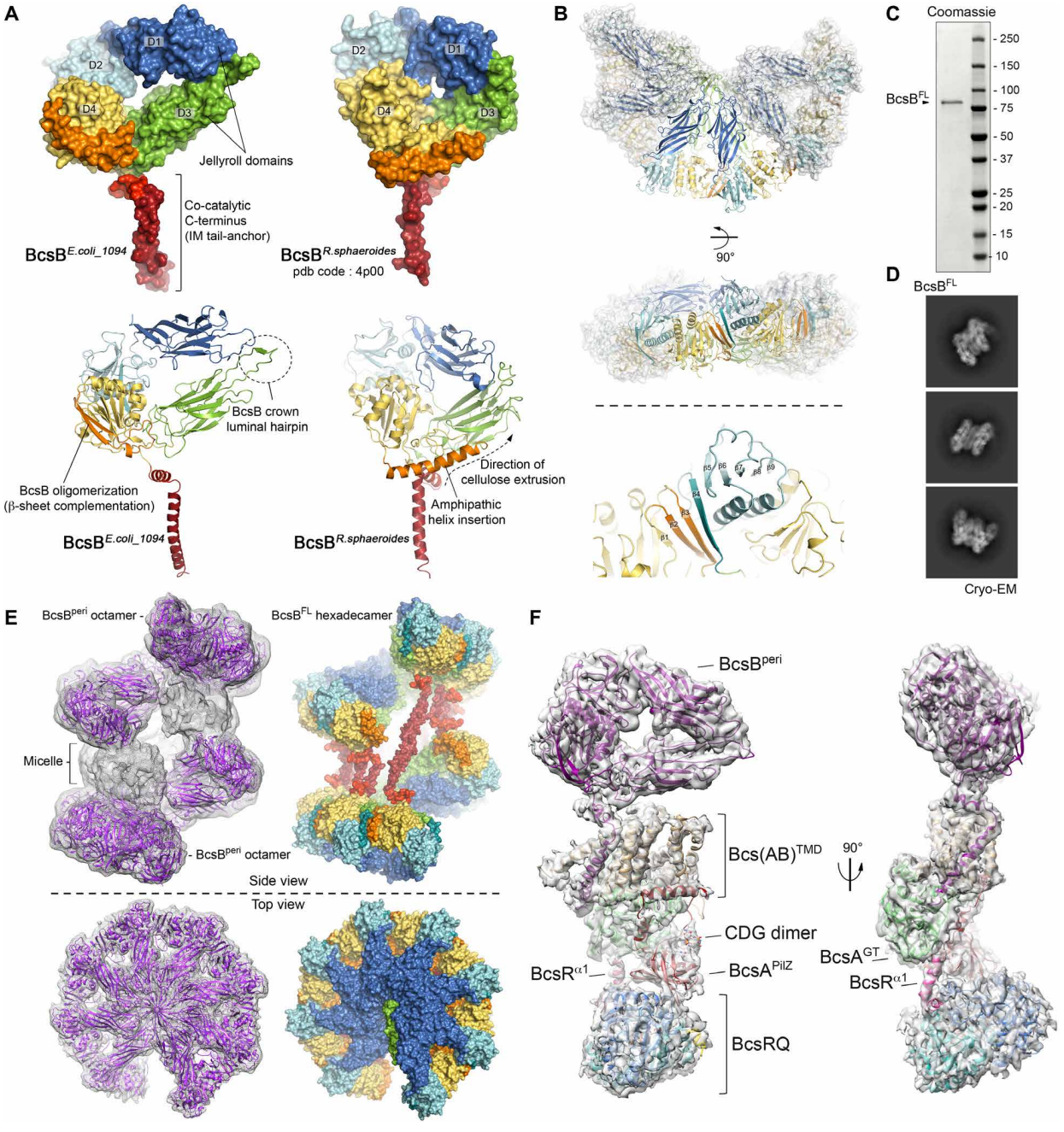

Fig. 2. Structure, polymerization, and asymmetry of the periplasmic crown and noncanonical BcsAB synthase tandem assembly. (**A**) Structural comparison of $BcsB^{FL}$ monomers from *E. coli* (left) and *R. sphaeroides* (right) shown in surface (top) and cartoon (bottom) representation in PyMOL. pdb, Protein Data Bank. (**B**) Top: A model of a hexameric BcsB crown derived from the refined $BcsB^{peri}$ pentamer in top and side views. Bottom: A close-up view of the nine-stranded β-sheet formed by β-sheet complementation between adjacent BcsB subunits. (**C**) Coomassie-stained SDS-PAGE of purified, detergent-extracted, full-length *E. coli* $BcsB^{His}$. (**D**) Cryo-EM 2D class averages of full-length $BcsB^{His}$. (**E**) Left: Cryo-EM density reconstruction of purified full-length $BcsB^{His}$ with density-fitted $BcsB^{peri}$ octamers. Right: A composite atomic model of the $BcsB^{FL}$ hexadecamer with visualized IM tail-anchors as observed in the BcsRQAB assembly. Color coding is as in (A). (**F**) Structure of the BcsRQAB assembly following particle subtraction and local refinement of the cryo–electron density. A single $BcsB^{peri}$ copy was fitted in the periplasmic region, and the amphipathic and transmembrane C-terminal helices were built in the refined density. A CDG-bound BcsA homology model was fitted in the transmembrane and membrane-proximal regions, and the polypeptide backbone was refined against the experimental density. A $BcsR_2Q_2$ crystal structure was fitted in the apical region as in Fig. 1. Separate structural modules and ligand molecules are indicated.

full-length $BcsB^{His}$ (Fig. 2, C to E) show that BcsB polymerization is both self-driven and self-limiting. The 3D reconstruction features two BcsB octamers embedded from opposite sites in a helical belt of detergent micelles (Fig. 2E). Whereas the $BcsB^{peri}$ regions refined to ~4.4-Å resolution following local refinement, the C-terminal BcsB anchors remained largely unresolved in the underlying detergent micelles. Nevertheless, in each of the two BcsB octamers, the periplasmic regions of the first BcsB copy contact the detergent micelle of the respective eight protomers and thus create a steric hindrance for further polymerization (Fig. 2E). Although the isolated $BcsB^{His}$ particles feature different transmembrane region content from the multicomponent Bcs macrocomplex, the intersubunit BcsB contacts remain virtually unchanged between the two assemblies (fig. S1G) and thus reinforce a model of superhelical, asymmetric crown polymerization driven by periplasmic β-sheet complementation. It is important to note that purified Bcs macrocomplex particles typically feature up to six BcsB copies in the crown, likely due to additional restrains on local membrane curvature and BcsB oligomerization potential imposed by interacting IM and cytosolic Bcs partners.

Noncanonical BcsAB synthase tandem assembly

BcsA and BcsB are often encoded by neighboring genes of the same operon and have been shown to engage in 1:1 interactions in both *Gluconacetobacter xylinus* and *R. sphaeroides* (*1*, *6*, *14*). Biochemical data have further shown that the C-terminal BcsB region, composed of an amphipathic and an IM α-helices, is absolutely necessary for glucose polymerization by both the *E. coli* and *R. sphaeroides* synthases in vitro (*8*). Last, structural studies on the $BcsAB^{R.sphaeroides}$ tandem have shown that the BcsB C-terminal anchor tightly associates with and completes the IM transport domain of BcsA, further supporting a structural and functional co-dependency between the subunits (*5*–*7*). On the basis of these data, we proposed earlier a similar 1:1 association between the co-catalytic partners in the assembled Bcs macrocomplex, but we could not distinguish between protein and detergent micelle densities in the negative-stain data (*4*). Unexpectedly, the cryo-EM structure reveals a single BcsA copy in the assembled Bcs macrocomplex (Figs. 1C and 2F), which forms a conserved BcsAB tandem with the membrane-proximal BcsB protomer, as determined by the relative position of the D3 luminal loops in the periplasm. On the other side of the membrane, BcsA folds, as expected, into a glycosyl transferase domain and a PilZ β-barrel module. A homology model could be fitted with minor adjustments into the electron density map [root mean square deviation (RMSD) of 1.6 Å over the Cα atoms between the Robetta (*15*) output and the density-refined model] and reveals extra density consistent with c-di-GMP binding to its canonical binding site onto the C-terminal PilZ module (Figs. 1C and 2F). Although these data suggest overall structural and functional conservation between the *E. coli* and *R. sphaeroides* BcsA homologs, the unexpected BcsA:BcsB stoichiometry, the proximity of a second c-di-GMP sensing protein (BcsE), and the direct interactions of BcsA with the essential for secretion BcsR and BcsQ subunits (see below) suggest that *E. coli* cellulose secretion is dependent on multiple additional regulatory inputs rather than a simple model of BcsAB tandem assembly.

Structural and mechanistic insights into the essential for secretion BcsRQ complex

BcsR is a short, 7-kDa polypeptide with unknown structure and function, whereas BcsQ is a 28-kDa protein predicted to belong to the ancient SIMIBI (signal recognition particle, MinD, and BioD) superfamily of pro- and eukaryotic nucleoside triphosphatases (NTPases). Members of the latter are key to a large variety of cellular processes including divisome positioning (MinD), bacterial flagellum secretion (FlhG and FlhF), and membrane protein sorting in both prokaryotes and higher organisms (SRP54-SR and Get3) (fig. S3) (*16*, *17*). We recently showed that BcsR and BcsQ exhibit chaperone-like function toward each other, where BcsR stabilizes BcsQ to form monodisperse $BcsR_2Q_2$ heterotetramers in solution, while BcsQ itself may play a role in the folding and subsequent stability of BcsR (*10*).

To increase the resolution of the apical BcsRQ subcomplex, we proceeded to protein crystallization. The BcsRQ complex crystallized in a variety of conditions and space groups, and several structures were solved at nearly atomic resolutions (1.6 to 2.1 Å; table S2), with only the ~10 C-terminal BcsQ amino acids remaining unresolved in the electron densities. The refined structural models feature a virtually unchanged conformation for BcsQ (RMSD of 0.19 to 0.42 Å over all atoms), whereas BcsR shows substantial flexibility in its N-terminal domain and the N-proximal end of helix α1.

BcsQ adopts a classical α-β-α SIMIBI NTPase fold with a central seven-stranded β-sheet (a ↑β7•↑β6•↑β1•↑β5•↑β2•↑β4•↓β3 core) sandwiched between flanking α helices (Fig. 3A and fig. S3A) (*18*). Regardless of the purification and crystallization conditions, BcsRQ crystallized as ATP-bound "sandwich" or "tango" dimers of heterodimers. In the latter, an extensive part of the BcsQ homodimerization interface is stabilized by a network of hydrogen bonds and salt bridges among residues from both BcsQ subunits, the "sandwiched" ATP moieties and multiple water molecules resolved in the electron density (Fig. 3, B and C). In particular, the adenine base is stabilized primarily by side-chain interactions with N^{171} in cis, whereas the triphosphate moiety interacts both with residues from the Walker A motif in cis (e.g., T^{16} and T^{17}) and with the side chains of N^{152} and R^{156} in trans (Fig. 3, C and D). Site-directed mutational analysis in cellulo shows that sandwich ATP binding is likely indispensable for cellulose secretion, as observed by the progressive reduction in calcofluor binding between the $BcsQ^{N152D}$, $BcsQ^{N152D•R156E}$, and $BcsQ^{N152A•R156A•N171A}$ mutants (Fig. 3E). Such ATP dependency is especially unexpected given the self-energized nature of cellulose biogenesis, which uses preactivated UDP-glucose as a substrate.

While ATP-dependent tango dimers are an essential part of the catalytic cycle of SIMIBI family members (fig. S3D), capturing them crystallographically has typically required either the introduction of hydrolysis-inactivating mutations or the use of nonhydrolysable ATP homologs and transition state mimics [reviewed in (*16*, *17*)]. In contrast, the dimer-of-heterodimers conformation appears to be the default state of purified BcsRQ (*10*) and the presence of the nucleotide triphosphate (NTP) in all $BcsRQ^{His}$ structures reveals the absence of nucleotide hydrolysis or exchange even after prolonged incubation periods or treatment with chelating agents (table S2). Consistent with this, the $Bcs^{His}RQ^{WT}$ complex exhibited only weak adenosine triphosphatase (ATPase) activity in vitro, which was further inhibited in the context of a $Bcs^{His}RQ^{WT}$-$BcsE^{217–523}$ heterocomplex (fig. S3).

A closer inspection of the BcsQ protein sequence and nucleotide-binding pocket reveals that the protein features a deviant P-loop or Walker A motif as well as an aspartate-to-cysteine (or serine) substitution at the catalytic water-activating residue at position 39 (Fig. 3D and fig. S4). In canonical SIMIBI NTPases, the P-loop typically features two lysine residues—K^{11} and K^{16} in MinD—which

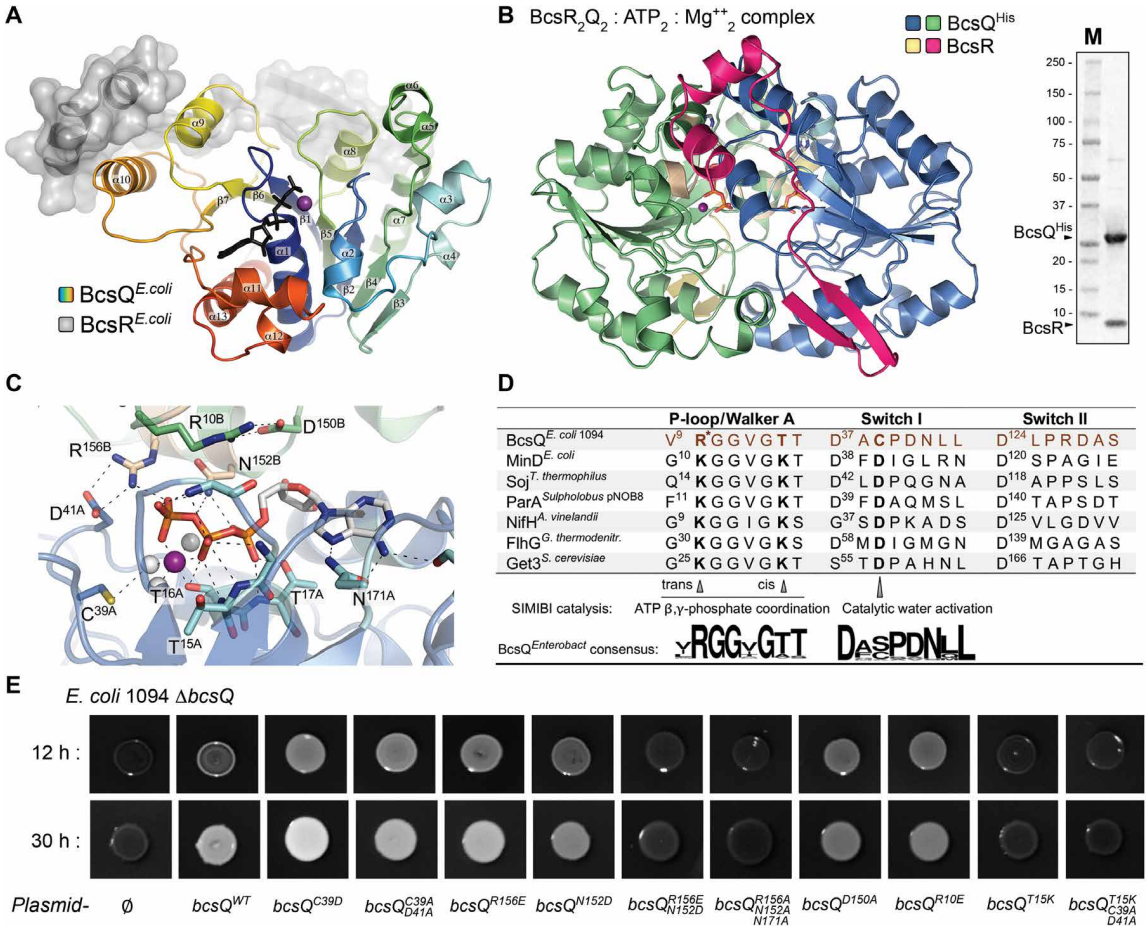

Fig. 3. Structural and functional analyses of the essential for cellulose secretion subunit BcsQ. (**A**) Structure of a BcsRQ^{His} heterodimer showing the conserved SIMIBI fold (in spectrum-colored cartoon), bound ATP (in black sticks), and Mg^{++} ion (as a purple sphere). (**B**) Crystal structure of the ATP-bound BcsRQ^{His} heterocomplex. Right: Coomassie-stained SDS-PAGE of the purified heterocomplex. (**C**) A close-up view of the ATP-binding pocket. BcsQ subunits are shown as cartoon in blue and lime, with ATP-coordinating residues colored in cyan and tan, respectively. Water molecules and the Mg^{++} ion are shown as gray and purple spheres, respectively. ATP and key surrounding residues are shown as sticks. (**D**) Primary sequence comparison of key functional motifs in canonical SIMIBI NTPases and enterobacterial BcsQ. (**E**) Functional complementation assay examining the role of key BcsQ residues in vivo. Colony cellulose secretion is evaluated by fluorescent calcofluor binding. Results are representative of at least six biological replicates. All BcsQ mutants were tested for protein expression and interactions with the BcsR and BcsE partners (E).

coordinate the phosphate moieties in trans and in cis, respectively, and are thought to aid electron density redistribution toward the phosphoanhydride bond oxygen during hydrolysis (Fig. 3D). In particular, the role of the K^{11} residue in trans is akin to that of the arginine finger in small guanosine triphosphatase (GTPase) activating proteins (GAPs), suggesting a common mechanism for intersubunit hydrolysis activation among NTPase superfamilies (*19*). The two lysines are typically key for SIMIBI protein function, as exemplified by *E. coli* MinD^{K11A} and MinD^{K16A} mutants, which are ATPase deficient and unable to interact with the downstream effector MinC (*18*).

In BcsQ, the cis-acting lysine is substituted by a threonine (T^{15}), which points away from the bound ATP and toward the core β-sheet (Fig. 3C). Mutation of this residue to the consensus lysine abolishes cellulose secretion in all tested contexts (BcsQ^{T15K} and BcsQ$^{T15K•C39A•D41A}$), which can be explained with altered geometry within the nucleotide-binding pocket rather than ATP hydrolysis activation. Although the purified Bcs^{His}RQ^{T15K} complex did not exhibit considerable ATPase activity in vitro, it showed ATP complexation, stability, and elution profiles similar to those of the wild-type BcsRQ complex. These data indicate that ATP binding and tango dimer formation alone are not sufficient for cellulose secretion and suggest an additional BcsQ-dependent step, possibly ATP hydrolysis, downstream of BcsERQ complex formation.

Further analysis of the nucleotide-binding pocket reveals that R^{10}, which corresponds to the consensus trans-acting Walker A lysine, is flipped away from the bound ATP and its conformation is stabilized by a salt bridge with the strictly conserved D^{150} from the same BcsQ subunit. Charge-reversal mutation of R^{10} (BcsQ^{R10E}) or, in contrast, a salt bridge–removal mutation of D^{150} that would release the Walker A arginine (BcsQ^{D150A}) lead both to decrease in calcofluor binding in vivo, indicating that the two interacting residues likely play a structural rather than a catalytic role in cellulose biogenesis. Instead of R^{10}, the role of arginine finger in BcsQ is taken by the tandem of conserved trans-acting residues N^{152} and R^{156}. While mutation of both residues leads to loss of cellulose secretion as mentioned above, a charge-reversal mutation of R^{156} (BcsQ^{R156E}) has actually stimulatory effects on cellulose secretion. It is important

to note that while the carboxamide nitrogen of N^{152} forms classical arginine finger interactions with the α-phosphate and the phosphoanhydride bond oxygen of the γ-phosphate, R^{156} coordinates the distal oxygen of the γ-phosphate and also engages into a salt bridge with the D^{41} residue in trans, which itself is in immediate proximity to the canonical catalytic water-activating residue at position 39 (Fig. 3C). The $BcsQ^{R156E}$ mutation could therefore have a twofold stimulatory effect with regard to putative downstream ATP hydrolysis: (i) A negative charge around the distal oxygens of the γ-phosphate would facilitate electron transfer from the attacking hydroxide nucleophile away from the distal oxygens and onto the phosphoanhydride bond oxygen, and (ii) a charge-reversal mutation of R^{156} would release its salt bridge partner D^{41} and increase the negative charge around active site–bound water molecules, therefore favoring water deprotonation and nucleophilic attack on the bound nucleotide. Consistent with this, purified $Bcs^{His}RQ^{R156E}$ exhibited stronger than wild-type ATPase activity in vitro. In addition, the injected protein sample eluted as several distinct species, consistent with BcsRQ complex disassembly, and coeluted nucleotide species did not concentrate together with the protein complex, further indicating nucleotide hydrolysis and release from the $Bcs^{His}RQ^{R156E}$ complex (fig. S3, F to H). Nevertheless, the apparent ATP hydrolytic activity of the $BcsQ^{R156E}$ mutant was inhibited in the context of a ternary $Bcs^{His}RQ^{R156E}$-$BcsE^{217–523}$ complex (fig. S3I), indicating that the BcsE regulator further stabilizes the ATP-loaded, precatalytic sandwich dimer formation.

Although the above results favor a hydrolytically active BcsQ protein, where ATP hydrolysis occurs downstream of the BcsERQ interactions in the context of cellulose biogenesis, it is less evident how the attacking nucleophile is initially activated. As mentioned above, the canonical water-deprotonating aspartate in switch I of the NTPase fold is substituted by a cysteine (C^{39}) or serine residue in enterobacterial BcsQ (Fig. 3D and fig. S4). Although the thiol side chains of cysteines can act as nucleophiles in enzymatic reactions, mutation of both C^{39} and the adjacent D^{41} to alanines ($BcsQ^{C39A•D41A}$) does not negatively affect calcofluor binding in vivo (Fig. 3). Nevertheless, a consensus-mimetic mutation ($BcsQ^{C39D}$) has a stimulatory effect on cellulose secretion, especially in the early stages of biofilm formation and even stronger than that of the $BcsQ^{R156E}$ mutation. The in vitro stability, ATPase activity, and nucleotide-loading states of the $Bcs^{His}RQ^{C39D}$ complex, however, are similar to that of the wild-type protein (fig. S3, F to H). Together, these data favor a model where BcsQ-bound ATP is hydrolyzed downstream of BcsRQ and BcsERQ complex formation, with catalytic water activation being mediated either in trans by a downstream binding partner or involving additional conformational changes within BcsQ to deliver an alternative water-deprotonating residue. In favor of this model, it is important to note that even canonical SIMIBI proteins are actually relatively poor ATPases. Rather, SIMIBI-dependent nucleotide hydrolysis typically requires membrane and/or effector binding and can involve either intrinsic to the NTPase amino acids or catalytic activation in trans by active site residues provided from downstream binding partners [e.g., lipid and MinE-dependent activation of MinD (*20*, *21*), Spo0J-dependent activation of Soj (*22*), and FlhG-dependent activation of FlhF (*23*)].

The crystal structures of the BcsRQ complex also reveal a possible mechanism for BcsR-dependent BcsQ stabilization. As reported recently, neither BcsR nor BcsQ can be purified as stable proteins when expressed separately, whereas BcsRQ coexpression leads to the purification of stable monodisperse $BcsR_2Q_2$ heterocomplexes. The crystal structures show that each BcsR polypeptide interacts stably with both BcsQ subunits (free energy gains of −21.4 and −9.4 kcal/mol) burying 1900 $Å^2$ of combined surface area (Fig. 4A and fig. S3, B and C). In particular, BcsR features a C-terminal V-shaped α-helical domain, $BcsR^{CTD}$, which effectively stitches the interface of the BcsQ homodimer by both polar and hydrophobic interactions, is required for cellulose secretion in vivo, and is sufficient for purification of a stable $Bcs^{ΔNTD}RQ$ heterocomplex (Fig. 4, A to D, and fig. S3, B and C). The interface occupied by $BcsR^{CTD}$ corresponds to the same interface occupied by MinE and Get1 in the MinDE and Get3-Get1 assemblies essential for divisome positioning and tail-anchored membrane protein sorting, respectively, indicating a common regulatory mechanism for cofactor association among SIMIBI family members (Fig. 4A) (*20*, *24*).

The remaining BcsR N-terminus ($BcsR^{NTD}$) features an extended conformation with an apical β-hairpin and adopts variable, partially disordered conformations among the six different crystal structures presented in this study (Fig. 4B). As we discussed recently, such conformational variability could have further stabilizing effects on BcsRQ complex assembly by minimizing the intrinsic aggregation propensity of BcsQ (*10*). Unexpectedly, while it is not requisite for BcsRQ complex formation (Fig. 4C), $BcsR^{NTD}$ appears to be crucial for cellulose secretion and BcsA biochemical detection in cells (Fig. 4, D and E). Fitting of the BcsRQ complex in the cryo-EM structures reveals that the two essential regulators occupy the apical density of the Bcs macrocomplex (Figs. 1C and 2F), with $BcsA^{PilZ}$ buttressing primarily one of the BcsQ subunits, whereas the α1 helix of the BcsA-proximal BcsR copy appears to extend at its N-proximal end to position $BcsR^{NTD}$ onto the catalytic glucosyl transferase domain, $BcsA^{GT}$ (Fig. 2F). Together, these data suggest additional regulatory roles for BcsR and BcsQ in synthase stabilization and activity regulation and can further explain the essential regulatory role of the protein heterocomplex in cellulose biogenesis in vivo.

Together, the cytosolic modules of the BcsARQE subunits enclose a large membrane-proximal vestibule within the Bcs macrocomplex, in which the regulatory $BcsA^{PilZ}$ module occupies a central position (Fig. 1C). Surface conservation analyses of the resolved BcsRQ and BcsRQ-BcsE assemblies (see below) indicate clustering of most conserved residues at the vestibule-facing side of the heterocomplexes (figs. S4 and S5), consistent not only with observed protein-protein interactions but also with the evolution of a specific local environment around the c-di-GMP sensing $BcsA^{PilZ}$ module and the gated catalytic $BcsA^{GT}$ domain. Conserved residues include a series of arginine (R^{174} and R^{201}) and glutamate (E^{203}) residues that adopt alternative conformations to form an electron-dense region at the bottom of the vestibule, which likely preclude nucleotide release and stabilize the tango dimer conformation, as well as composite c-di-GMP sensing sites on the partner BcsE protein, which likely contribute to activating dinucleotide retention for processive glucose polymerization (below).

Structural analyses of the BcsRQ-BcsE interactions and multisite c-di-GMP complexation

We recently showed that BcsE features a tripartite architecture, namely, an N-terminal RecA ATPase-like module ($BcsE^{NTD}$), followed by a phosphotransfer incompetent receiver ($BcsE^{REC*}$) domain and a catalytically inactive GGDEF module ($BcsE^{GGDEF*}$) (*10*). We further showed that while the N-terminal domain oligomerizes in head-to-tail

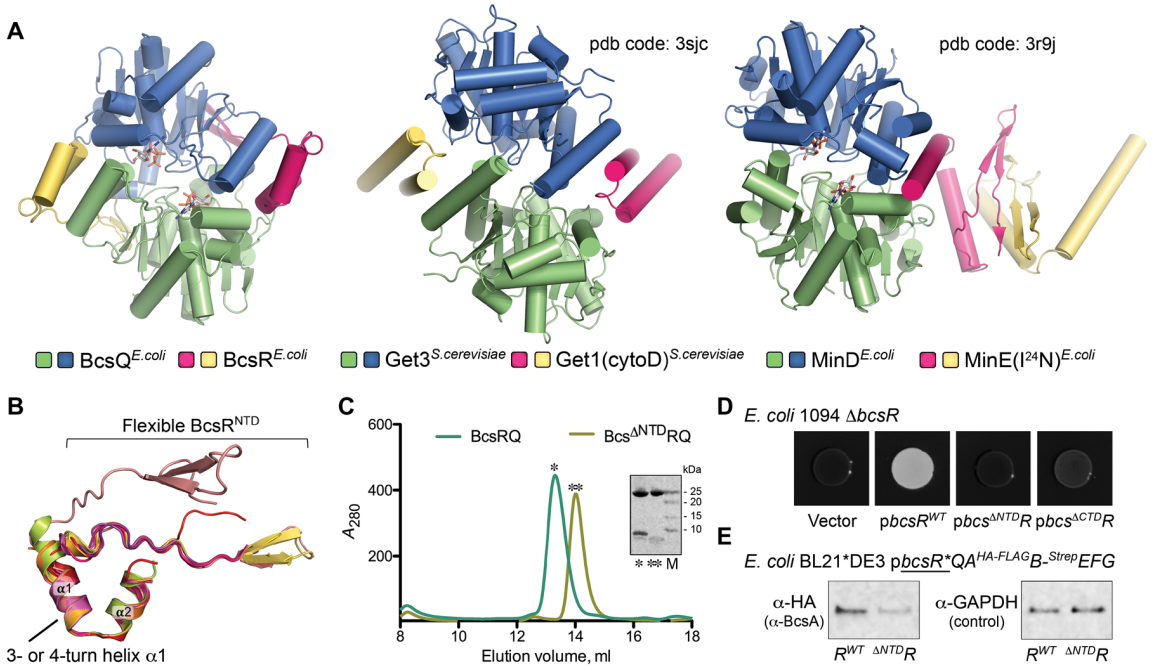

Fig. 4. Structural and functional analyses of the essential for cellulose secretion subunit BcsR. (**A**) Comparison of the BcsRQ complex with two-component complexes of SIMIBI superfamily members. (**B**) Overlay of BcsR subunits found in the asymmetric units of all structures resolved in this study. (**C**) Size exclusion chromatography and SDS-PAGE analysis of purified BcsRQ and Bcs$^{\Delta NTD}$RQ. Molecular weights for the tag-free BcsR and Bcs$^{\Delta NTD}$R are 7.4 and 3 kDa, respectively. (**D**) Functional complementation assay of the role of BcsR domains in cellulose secretion in vivo. Results are representative of at least six biological replicates. (**E**) Western blot detection of cellular BcsA upon Bcs macrocomplex expression in the context of BcsR^{NTD} deletion [GAPDH, glyceraldehyde-3-phosphate dehydrogenase (loading control)]. The results are representative of at least three replicates.

manner and participates in BcsF-driven recruitment of BcsE to the membrane, the C-terminal BcsE^{GGDEF*} moiety is responsible for binding of both dimeric c-di-GMP and BcsQ (*10*). On the basis of these data, we can unambiguously assign the membrane-proximal electron-dense region that lies across from BcsA and underneath the membrane-distal crown repeats to a BcsE^{NTD} dimer (Fig. 2B), but overall, the cryo-EM reconstruction fails to provide further structural insights into the BcsERQ regulatory complex assembly.

To overcome this, we proceeded to purify and crystallize stable BcsRQE* complexes. We obtained crystals for two multicomponent assemblies, BcsRQE$^{349–523}$ and BcsRQ^{R156E}E$^{217–523}$, which diffracted to nearly atomic resolution and yielded structural models refined to 2.5 and 2.9 Å, respectively (table S3). Within the two structures, crystallized in the presence of c-di-GMP and AppCp/Mg^{2+}, the BcsQ dimers are largely unchanged from the those observed in the isolated BcsRQ complexes (RMSD over all atoms < 0.41 Å). The most substantial conformational change from the latter is observed in one of the BcsR copies in the BcsRQ^{R156E}E$^{217–523}$ structure, where the α1 helix features an additional turn at its N-proximal end and the remaining N-terminal region is flipped away from the complex to wrap along a BcsQ protomer from a symmetry-related assembly. This is reminiscent of the apparent conformation of the BcsA-proximal BcsR copy in the cryo-EM reconstruction, where the protein's N-terminal region is flipped away from BcsQ and appears to extend onto the synthase's glycosyl transferase module (Figs. 1C and 2F).

The two crystal structures reveal that BcsE binds BcsQ through a composite interface (1490 Å^2, free energy gain of −9.1 kcal/mol), including a nonlinear binding surface on the GGDEF* module distal from both the c-di-GMP–bound I-site and the N-proximal REC* domain, as well as an extended interface of 1055 Å^2 formed by the ~40 C-terminal residues of BcsE (BcsE^{CT}) (Fig. 5A and fig. S6, A to D). The latter are unresolved in the crystallized BcsE$^{217–523}$ construct alone (*10*), suggesting BcsQ-mediated tertiary structure stabilization. The interface is stabilized by both polar and hydrophobic interactions and particularly by conserved Pro and Leu residues (P^{515} in the enterobacterial consensus/P^{509} in BcsE$^{E.coli}$ and L^{520} in the consensus/L^{514} in BcsE$^{E.coli}$) plugging into two hydrophobic pockets onto the BcsQ surface (fig. S6C). Although deletion of the C-terminal tail or the globular GGDEF* module alone abolishes stable BcsERQ complex purification (fig. S6F), the bipartite interface may allow substantial flexibility in the relative orientations of the BcsQ and BcsE^{GGDEF*} modules in the context of a secretory assembly stabilized by additional protein-protein interactions.

In addition to revealing the structural determinants for BcsQ recruitment, the two BcsRQE structures provide unexpected insights into activating c-di-GMP complexation. Consistent with solution biophysical data (*10*), c-di-GMP is found bound as an intercalated dimer to each GGDEF* domain, partaking in canonical interactions with the conserved R^{415}xxD I-site motif. However, in the BcsRQ^{R156E}E$^{217–523}$ complex, the interstitial α_i helix and the BcsE^{REC*} module of BcsE undergo drastic conformational change [144° rotation and 45 Å displacement relative to the recently reported BcsE$^{217–523}$–c-di-GMP structure (*10*)] to contribute a second conserved RxxD motif (R^{306}ATD), which forms virtually identical I-site–like interactions with the second c-di-GMP molecule (Fig. 5, C and D). We further show that although this second I-site is insufficient for stable c-di-GMP recruitment alone (*10*), it drastically stabilizes the binding of dimeric c-di-GMP in solution as demonstrated by the

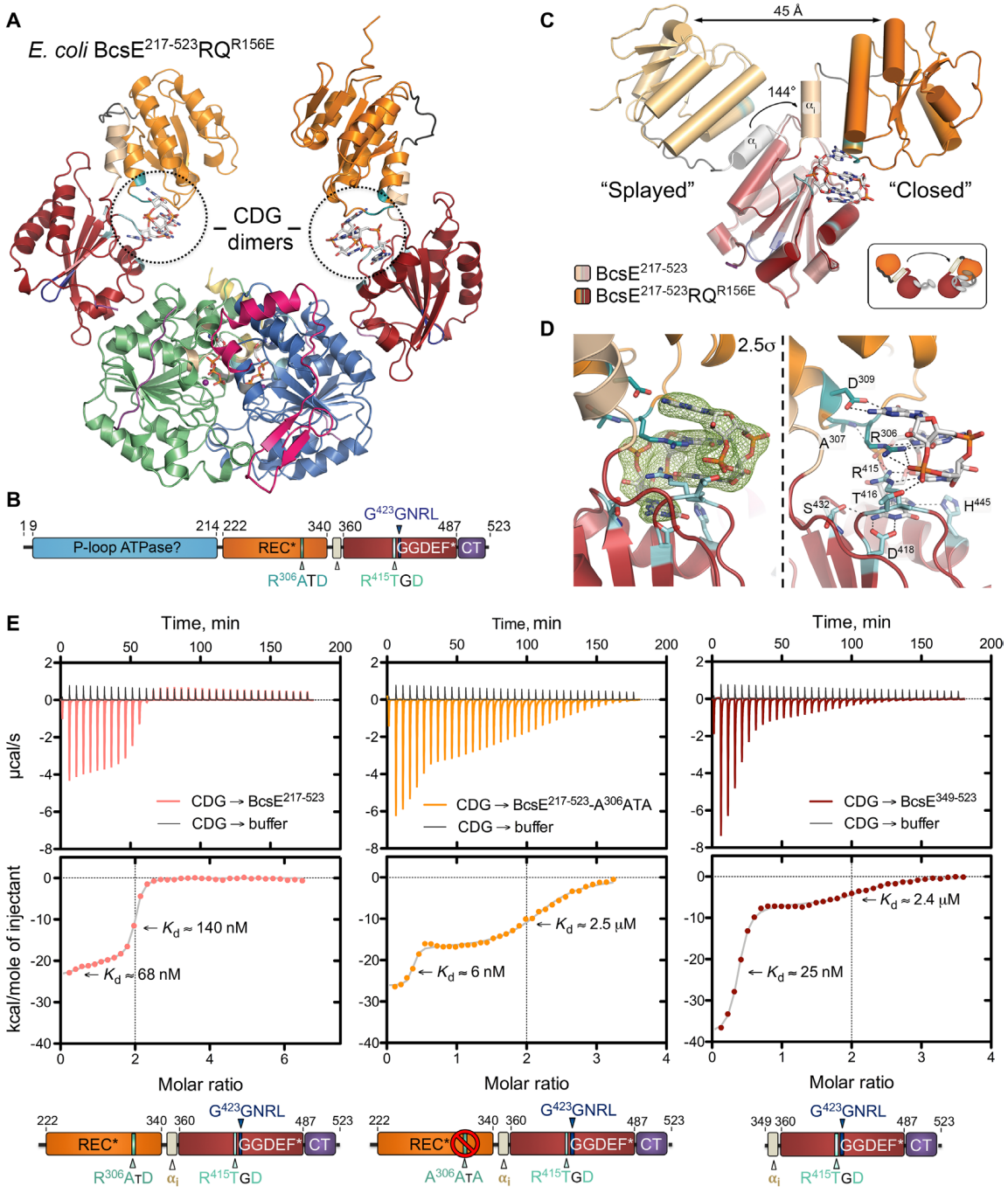

Fig. 5. Multisite c-di-GMP recognition and structure of the BcsRQ^{R156E}-BcsE$^{REC*-GGDEF*}$ complex. (**A**) Crystal structure of untagged BcsRQ^{R156E}-E$^{217–523}$ assembly in complex with ATP/ACP (β,γ-methyleneadenosine triphosphate or AppCp) and c-di-GMP. (**B**) Full-length BcsE domain architecture and functionally validated c-di-GMP–binding motifs (RxxD I-sites I and II) as identified in this study. (**C**) Captured conformational changes in the BcsE$^{REC*-GGDEF*}$ tandem between the BcsE$^{217–523}$ ["Splayed" (*10*)] and BcsRQ^{R156E}E$^{217–523}$ ("Closed") crystal structures. (**D**) Close-up views of c-di-GMP complexation in the three-component complex. Left: An $|F_o|$-$|F_c|$ partial electron density map calculated from a model before inclusion of the dinucleotide and contoured at 2.5 σ. Right: A cartoon-and-stick representation of c-di-GMP coordination. Canonical I-site I residues are colored in cyan; secondary I-site II residues are colored in teal. (**E**) Functional validation of the secondary I-site on the BcsE^{REC*} module (R^{306}ATD) by isothermal titration calorimetry. K_d values were calculated using a two-site binding model.

altered thermodynamic profiles of c-di-GMP binding to truncated (BcsE$^{349–523}$) or point-mutant (BcsE$^{217–523}$•A^{306}ATA) variants (Fig. 5E). As the processive transfer of glucose moieties onto the nascent cellulose chain requires recurrent opening of BcsA's active site by dimeric c-di-GMP binding to the protein's PilZ module, synthase-proximal enrichment of the dinucleotide in already intercalated conformation by the BcsE$^{REC*-GGDEF*}$ tandem can have direct functional implications in the context of an assembled secretion macrocomplex.

Furthermore, although c-di-GMP binding to receiver domains has been reported earlier, the dinucleotide binding mode in $BcsE^{REC*}$ is markedly different. For example, we first reported c-di-GMP recognition by *Vibrio cholerae* VpsT, where the degenerate receiver domain features a C-terminal α-helical extension (α6) through which it dimerizes to form an intersubunit c-di-GMP binding pocket (*25*). Similarly, some CheY-like response regulators have been reported to bind c-di-GMP through an arginine-rich C-terminal extension of the canonical REC domains, the corresponding peptide alone being sufficient for ligand complexation (*26*). However, to our knowledge, BcsE is the first example where a REC domain fold contributes an intrinsic, I-site–like motif for c-di-GMP coordination.

In addition to the second I-site, the $BcsRQE^{349–523}$ structure reveals a third crystallographic, c-di-GMP–binding motif (fig. S6, F to I). In particular, the dinucleotide dimer bound to the $BcsE^{GGDEF*}$ I-site of a symmetry-related BcsE molecule ($BcsE^{SYM}$) is further coordinated by multiple π-stacking and polar interactions with residues from cognate BcsE ($R^{503}H^{504}$), BcsR ($R^{51}W^{52}$), and BcsQ (R^{219}) protomers (fig. S6G). Although it is not evident that this third binding site has biological relevance in cellulose secretion, its proximity to the $BcsA^{PilZ}$ module raises the possibility of it contributing additional weak interactions for synthase-proximal dinucleotide retention in vivo.

Last, the $BcsRQ^{R156E}E^{217–523}$ structure also provides a structural basis for the poor resolution and likely conformational heterogeneity of the BcsE-corresponding regions in the cryo-EM density reconstruction. Namely, $BcsE^{217–523}$ features substantial changes in the relative orientation of the REC* domain relative to the GGDEF* module when compared not only between the $BcsE^{217–523}$ and $BcsRQ^{R156E}E^{217–523}$ structures (144° rotation, 45-Å displacement) but also between $BcsE^{217–523}$ subunits in the asymmetric unit of the three-component crystal structure alone (20.4° rotation, 6.25-Å displacement). As even local refinement of the cryo-EM data failed to yield electron densities into which we can reliably fit the crystallographic structures, we have refrained from proposing a specific model for the 3D organization of the $BcsE^{REC*\text{-}GGDEF*}$ modules in the context of the assembled Bcs macrocomplex.

DISCUSSION

Apart from some cyanobacteria, all cellulose-producing bacteria feature a BcsAB tandem as the catalytic core of their cellulose biosynthetic machineries (*1*). The latter can be classified in three major types, as found in *G. xylinus* (type I), *E. coli* (type II), and *Agrobacterium tumefaciens* (type III) (*1*). Most of the structural information on the catalytic subunits has come from studies of the BcsAB homologs from *R. sphaeroides*, an organism that features a type I cellulose secretion apparatus (*1*, *6*, *7*). As *R. sphaeroides* secretes amorphous cellulose and no evidence for BcsAB polymerization has been found in vitro or upon analysis of crystallographic interfaces (*4*), it is likely that the *R. sphaeroides* biosynthetic modules consist of separate BcsAB heterodimers in cellulo. In contrast, we showed previously that *E. coli* BcsB likely features polymeric organization in the membrane as seen in detergent-extracted and not reconstituted Bcs macrocomplexes studied by single-particle electron microscopy in negative stain (Fig. 1A) (*4*). Here, we provide nearly atomic resolution data showing that BcsB polymerizes via a β-sheet complementation mechanism among subunits and propose that polymerization would be limited by both the membrane surface tension and the transmembrane domains (TMDs) of interacting Bcs subunits, such as the BcsB membrane anchors, BcsA's transport domain on one side, and, likely, BcsE-interacting BcsF copies on the other side of the crown. Whereas BcsB features a high degree of overall sequence and surface conservation, the D2:D4 β strands and the stacked luminal loops that mediate intersubunit β-strand addition feature relatively low sequence conservation, consistent with the fact that the observed β-strand interactions are backbone-mediated and mostly side-chain independent (figs. S2, B to E, and S5).

Both the D2:D4 intersubunit interactions and the D3 luminal loops appear conserved at the secondary structure level among enterobacteria but are absent in the *R. sphaeroides* BcsB homolog, where D4 features a long amphipathic α-helix insertion in lieu of the interfacial β strand (Fig. 2A and fig. S2) (*6*). This can explain the monomeric conformation of *R. sphaeroides* BcsB and compels the question of whether the absence of a D4 amphipathic helix insertion and an *E. coli*–like predicted secondary structure can be used as a molecular marker for BcsB oligomerization. For example, in *G. xylinus*, which features a type I cellulose secretion machinery and where c-di-GMP and its effect on cellulose biosynthesis were first found (*27*), immunolabeling on freeze-fractured cells has shown that the Bcs complexes arrange in a linear row along the cell surface (*28*). Primary and secondary structure alignments show that $BcsB^{G.xylinus}$ is more akin to the *E. coli* rather than the *R. sphaeroides* BcsB homolog (i.e., presence of putative interfacial β-strand motifs and lack of amphipathic helix insertion), which raises the possibility that the peculiar supramolecular organization of cellulose synthesis in *G. xylinus* could be, at least partly, driven by intermolecular BcsB interactions.

In addition to a conserved BcsB polymerization mechanism, the cryo-EM Bcs macrocomplex reconstruction also revealed a noncanonical BcsA:BcsB stoichiometry that differs substantially from a generally accepted model of equimolar synthase tandem assembly (Fig. 1C). The altered BcsA:BcsB ratio is also particularly interesting, as it demonstrates a biosynthetically expensive stoichiometry for a complex that features a single catalytic subunit. Possible roles for the BcsB polymeric crown might include local perturbations of the IM for facilitated BcsA membrane sorting or function, a ratchet-like organization of the BcsB crown lumen for more efficient cellulose extrusion, a supramolecular assembly for recruitment of regulatory enzymes [e.g., the hydrolase BcsZ, the pEtN transferase BcsG, or BcsB-interacting c-di-GMP metabolizing enzymes PdeK and DgcC (*1*, *9*, *29*)], periplasmic peptidoglycan rearrangements for facilitated guidance toward the outer membrane export channel, or introduction of overall secretion system asymmetry related to the role of the essential SIMIBI subunit BcsQ (see below). Furthermore, the link between BcsB oligomerization and membrane deformation could also explain preferential secretion system assembly at the cell pole (*11*), where the native membrane curvature is inherently highest.

As mentioned above, cellulose secretion in *E. coli* is absolutely dependent on the small cytosolic subunits BcsR and BcsQ [Figs. 3 and 4 and (*4*)]. The structural and functional analyses of the BcsRQ heterocomplex presented here reveal multiple parallels with the structure and mechanism of canonical SIMIBI proteins, which are important multistate regulators in a variety of cellular functions (fig. S3D). An important feature of SIMIBI proteins is the uncoupling of NTP-dependent dimerization and hydrolysis, which provides an additional spatiotemporal control of the proteins' function. The data presented here support a similar model of delayed, dimerization-uncoupled, BcsQ-dependent ATP hydrolysis within the

Bcs secretion system, which occurs downstream of the BcsRQE regulatory complex assembly. Given the substantial effects of BcsQ and BcsR on the detectable levels of IM BcsA [(*4*) and Fig. 4E] and that the BcsERQ complex is recruited to the membrane upon expression of IM BcsF (*10*), it is possible that the BcsRQ tandem plays a direct role in the membrane sorting and/or stability of the BcsA synthase similar to the function of other protein-sorting SIMIBI NTPases [e.g., the SRP54-SR tandem for general membrane protein sorting, Get3 for TA-protein insertion, and FlhF for flagellum assembly initiation (*16*, *17*, *23*)]. As the BcsRQ complex is secretion system specific and involves interactions with a single BcsA copy, it would require no nucleotide or protein recycling mechanisms but rather partake in an energetically economical "one-shot" Bcs macrocomplex assembly.

Although the precatalytic ATP-bound tango dimers of SIMIBI proteins are typically pseudosymmetric, they often participate in asymmetric protein-protein interactions along their catalytic cycles (*16*, *17*). For example, studies on the MinD-MinE complex have shown that the MinE dimer cannot simultaneously affect both catalytic sites of the MinD homodimer and that asymmetric binding of MinE is sufficient to trigger ATP hydrolysis and membrane release of MinD (*20*, *21*). Similarly, in tail-anchored protein sorting homodimeric, guanosine triphosphate (GTP)–loaded Get3 forms an asymmetric complex with the Get4-Get5 partners to secure efficient cargo loading before its delivery to the membrane through GTP hydrolysis, interactions with the Get2-Get1 insertase complex, nucleotide release, and Get3 recycling (*16*, *17*). Similar functional asymmetry is also observed in the assembled Bcs macrocomplex. In particular, the apical BcsRQ subcomplex buttresses a single BcsA copy, where most of the contacts are between the $BcsA^{PilZ}$ domain and a single BcsQ subunit, whereas the N-terminal domain of the proximal BcsR chain appears to extend past the PilZ module and onto the catalytic glycosyl transferase domain. Overall secretion system asymmetry is also secured by the superhelical polymerization of BcsB discussed above, as well as by the substantial conformational flexibility of partner BcsE.

Regarding the role of the third cytosolic regulator BcsE, we recently showed that the protein features an unexpected tripartite architecture composed of degenerate (*) NTPase, REC, and GGDEF domains and that it participates in both secretion system assembly through high-affinity interactions with BcsF and BcsQ and activating cofactor complexation through binding of c-di-GMP to the conserved GGDEF* domain I-site (R^{415}TGD). Here, we demonstrate the contribution of a second I-site (R^{306}ATD), intrinsic to the REC* domain, that stabilizes binding of the dinucleotide in its synthase-activating intercalated dimer form at the REC*-GGDEF* interface (Fig. 5). Both the cryo-EM data and crystallographic structures attest to substantial structural variability between the two modules that could reflect conformation-dependent c-di-GMP binding affinities. In a functional mechanism where dimeric c-di-GMP migrates in and out of the $BcsA^{PilZ}$ domain to allow substrate entry at each cycle of processive glucose polymerization (*5*), BcsE could thus contribute to the retention of a synthase-proximal pool of activating dinucleotide that is made available through minor conformational changes. Last, the tandem $BcsE^{REC*\text{-}GGDEF*}$ I-sites (Fig. 5), the observation of a third crystallographic site for c-di-GMP recognition at the interface of BcsR, BcsQ, and BcsE protomers (fig. S6, F to I), the conspicuous conservation of the vestibule-lining protein surfaces (fig. S5), and the discovery of colocalizing, secretion system–specific, c-di-GMP–metabolizing enzymes (*29*) all point toward *E. coli*–like cellulose secretion evolution toward intersubunit cooperativity and limited dinucleotide diffusion.

MATERIALS AND METHODS

The experiments were not randomized and the investigators were not blinded during experimental design, execution, or outcome assessment. However, most experiments were reproduced independently by different investigators, including crystallographic, biochemical, biophysical, and phenotypic functional assays.

Bacterial strains

Plasmids for recombinant protein expression (see below) were propagated in and isolated from *E. coli* DH5α cells. All recombinant protein expression for structural and in vitro biochemical studies was carried out in BL21(DE3) Star cells, including the expression of selenomethionine-derivatized proteins. *E. coli* 1094 Δ*bcsQ* or Δ*bcsR* strains were used in complementation phenotypic assays with *bcsQ* or *bcsR* variants, respectively, expressed from a low-copy isopropyl-β-D-thiogalactopyranoside (IPTG)–inducible vector (pAM238, below). All bacterial strains and plasmids used in this study are available upon request.

Recombinant DNA techniques

DNA manipulations were carried out using standard protocols for polymerase chain reaction (PCR), molecular cloning, transformation, and DNA analysis. Coding regions for BcsR, BcsQ, BcsRQ, BcsRQAB, BcsE, and BcsEFG variants were amplified using *E. coli* 1094 genomic DNA as a template and a high-fidelity DNA polymerase (Phusion, New England Biolabs) and inserted via digestion/ligation cloning into IPTG-inducible expression vectors with custom-modified multiple cloning sites (MCSs). Point mutations, insertion of stop codons, MCS modifications, and domain deletions were performed using inverse PCR-based protocols and mutation-specific oligonucleotides as primers. All recombinant vectors and introduced mutations were verified by DNA-sequencing and, where applicable, IPTG-inducible protein expression. All BcsQ mutants tested in phenotypic functional assays were verified for expression and copurification with the rest of the $BcsE^{217–523}$RQ complex components.

Protein expression and purification

As BcsR and BcsQ fail to express or purify stably when cloned separately, all variants of the BcsRQ complex were purified following protein coexpression and not complex reconstitution. In particular, the coding region corresponding to the BcsRQ tandem (as found in operon) was amplified and cloned into both the pProExHTB and pET21b expression vectors, adding a cleavable N-terminal or non-cleavable C-terminal hexahistidine tag to BcsR (pProExHTB-^{His}RQ) or BcsQ (pET-RQ^{His}), respectively (*10*). For coexpression purposes, the coding regions corresponding to $BcsE^{217–523}$ and $BcsE^{349–523}$ were cloned into custom-modified pRSFDuet1* expression vector under control of the first T7 promoter, as reported recently (*10*). Overexpression of the Bcs macrocomplexes was performed as previously (*4*) by coexpression of the pCDFDuet1-$Bcs^{His}RQA^{HA\text{-}FLAG}B$ and pRSFDuet1*-^{Strep}EFG constructs after introduction of targeted modifications. Last, for $BcsB^{FL}$ expression, the corresponding coding region was cloned using Nde I/Not I–based restriction/ligation

protocol into a pET21b vector to yield a C-terminally hexahistidine-tagged protein upon recombinant overexpression.

For protein purification, all expression vectors were (co-)transformed into chemically competent *E. coli* BL21(DE3) Star cells. For the expression of native proteins, cells were grown at 37°C under aerobic conditions in terrific broth medium supplemented with appropriate antibiotics [ampicillin (100 μg/ml), kanamycin (40 μg/ml), or a combination of ampicillin (70 μg/ml) + kanamycin (30 μg/ml) for coexpressed vectors]. At a cell optical density corresponding to an absorbance of 0.8 to 1.0 at 600 nm (OD_{600}), the cells were moved to 17°C and overnight protein expression was induced by the addition of IPTG at a final concentration of 0.7 mM. For the expression of selenomethionine-derivatized proteins, 4 liters of cells was initially grown at 37°C in LB medium to an OD_{600} of 0.5 to 0.6. Cells were then pelleted by centrifugation (4000*g*, 15 min, 20°C), gently washed with 200 ml of 1× SelenoMet Medium Base (Molecular Dimensions), collected again, and resuspended in 1 liter of complete SelenoMet Medium (Molecular Dimensions) supplemented with L-selenomethionine (40 mg/liter) and the appropriate antibiotic. Cells were then grown for an additional hour at 37°C, transferred to 17°C, and induced with IPTG as above.

After 16 hours, cells were harvested by centrifugation, resuspended in lysis buffer, and flash-frozen in liquid nitrogen. For BcsRQ purification, the composition of the lysis buffer was 20 mM Hepes (pH 8.0), 120 mM NaCl, 19 mM imidazole (pH 8.0), 2 mM β-mercaptoethanol, and cOmplete protease inhibitors (1 tablet/50 ml) (Roche). For the $BcsRQ^{R156E}$-$BcsE^{217–523}$ and BcsRQ-$BcsE^{349–523}$ complexes, the immobilized metal affinity chromatography (IMAC) buffer was also supplemented with 0.5 μM c-di-GMP (Jena Bioscience or Sigma-Aldrich), 2 μM AppCp (Jena Bioscience), 5 mM $MgCl_2$, and 10% glycerol.

For protein purification, cells were thawed and lysed using an EmulsiFlex-C3 high-pressure homogenizer (Avestin). Cell debris were removed by centrifugation (1 hour at 50,000*g* and 4°C), and the cleared lysates were loaded onto buffer-washed Talon Superflow resin (GE Healthcare) at approximately 0.5 to 1 ml of resin/liter of culture. The resin was subsequently washed with more than 20 volumes of IMAC buffer A (protease inhibitor–free lysis buffer as above), and bound proteins were eluted in a single step with IMAC buffer A supplemented with 200 mM imidazole (pH 8.0) (IMAC buffer B).

For purification of $BcsRQ^{His}$, eluted protein was supplemented with 15 mM EDTA (pH 8.0), concentrated to 2.5 ml using an Amicon Ultra centrifugal filter (30-kDa cutoff; Millipore), and desalted using a disposable PD-10 desalting column (GE Healthcare) and IMAC buffer A. The protein fraction was then incubated with 5 mM $MgCl_2$ and excess AppCp (1 mM), adenosine diphosphate (ADP; 1 mM), or no nucleotide and subjected to size exclusion chromatography on a Superdex 200 Increase 10/300 GL column (GE Healthcare) equilibrated in gel filtration buffer [20 mM Hepes (pH 8.0), 120 mM NaCl, and 2 mM dithiothreitol (DTT)]. Collected protein fractions were analyzed for purity by SDS–polyacrylamide gel electrophoresis (SDS-PAGE), pooled, concentrated, flash-frozen in liquid nitrogen, and stored at −80°C. For purification of untagged $Bcs^{\Delta NTD}RQ$ complex, the coding region covering residues 40 to 62 of BcsR and full-length BcsQ were cloned into a pProExHTB vector and IMAC-purified in parallel to the full-length BcsRQ complex as above. The eluted complexes were desalted for imidazole removal and incubated overnight with His-tagged viral HRV-3C protease for cleavage of the N-terminal hexahistidine tag on BcsR. Following reverse IMAC for protease and tag removal, the flow-through fraction was concentrated and subjected to size exclusion chromatography (SEC). The eluted fractions were analyzed by SDS-PAGE, concentrated, flash-frozen, and stored at −80°C. Molecular weights for the full-length BcsR and $Bcs^{\Delta NTD}R$ following tag cleavage are 7.5 and 3 kDa, respectively.

Complexes $BcsRQ^{R156E}$-$BcsE^{217–523}$ and BcsRQ-$BcsE^{349–523}$ were purified in a similar two-step IMAC procedure. After tag removal, the proteins were subjected to SEC using a Superdex 200 Increase 10/300 GL column and gel filtration buffer with composition 20 mM Hepes (pH 8.0), 120 mM NaCl, 5 mM $MgCl_2$, 0.5 μM c-di-GMP, 2 μM AppCp, 2 mM DTT, and 10% glycerol. Collected protein fractions were analyzed for purity and stoichiometric complex assembly, concentrated, and flash-frozen in liquid nitrogen for storage at −80°C.

Expression of the Bcs macrocomplex (pCDFDuet1-$Bcs^{His}RQA^{HA-FLAG}B$ + pRSFDuet1*-$^{Strep}EFG$) was performed as reported previously (*4*). Briefly, after cotransformation, culture growth, induction and overnight expression, cells were pelleted by centrifugation and resuspended in ice-cold lysis buffer containing 20 mM Hepes (pH 8.0), 120 mM NaCl, 10% glycerol, 5 mM $MgCl_2$, 2 μM AppCp, 2 μM c-di-GMP, 250 μM cellobiose, lysozyme (100 μg/ml), and cOmplete EDTA-free protease inhibitors (1 tablet/50 ml) (Roche). After lysis (EmulsiFlex-C3), cell debris were removed by low-speed centrifugation (12,000*g*, 15 min, 4°C) and the membranes were pelleted by ultracentrifugation using an SW 28 Ti Beckman rotor (26,500 rpm or up to 126,000*g* for 1 hour at 4°C). After removal of the supernatant, the membrane fraction was resuspended in solubilization buffer containing all lysis buffer components but lysozyme and cellobiose, as well as a mix of detergents at the following final concentrations: 0.4% (w/v) digitonin (Sigma-Aldrich), 0.4% (w/v) *n*-dodecyl-β-D-maltopyranoside (anagrade β-DDM, Anatrace), 0.4% (w/v) decyl maltose neopentyl glycol (DM-NPG; Anatrace), and 0.2% lauryl maltose NPG (LM-NPG; Anatrace). After a 60-min incubation at 17°C and under mild agitation, the solubilized membrane fraction was cleared by a second high-speed centrifugation step as above. The supernatant was then incubated with anti-FLAG M2 affinity gel (50 μl of packed resin per liter of induced culture; Sigma-Aldrich) under mild agitation at 4°C for 1 hour. After gravity elution of the nonbound fraction, the resin was washed extensively (>30 column bed volumes) with binding buffer containing all lysis buffer components but lysozyme and cellulase, as well as 0.008% (w/v) LM-NPG. The bound complexes were then eluted using four column bed volumes of elution buffer (affinity buffer supplemented with 3× FLAG peptide at 100 μg/ml) and concentrated on a 100-kDa cutoff Amicon Ultra (Merck Millipore) centrifugal filter. For cryo-EM grid preparation, the Bcs macrocomplex was eluted in a glycerol-free buffer, concentrated to ~0.8 mg/ml, spotted on glow-discharged gold Quantifoil grids, blotted, and plunge-frozen in liquid ethane using a Vitrobot Mark IV device (Thermo Fisher Scientific) at 4°C and 100% humidity.

For BcsA detection in the context of N-terminally truncated BcsR ($Bcs^{\Delta NTD}R$), expression of the corresponding Bcs macrocomplexes was performed as above. To avoid overnight saturation effects, expression was IPTG-induced at 37°C and $BcsA^{HA-FLAG}$ detection was analyzed 120 min after induction. Glyceraldehyde-3-phosphate dehydrogenase (GAPDH) detection was used as loading control for the experiments.

Last, $BcsB^{FL}$-overexpressing BL21(DE3)* cells were pelleted and resuspended in buffer containing 20 mM Hepes (pH 8.0), 500 mM NaCl, 19 mM imidazole (pH 8.0), and 10% glycerol and lysed by sonication. Nonlysed cells were removed by a 15-min centrifugation at 12,000*g*, and the supernatant was collected. The sample was then mixed with detergents at final concentrations of 0.4% β-DDM, 0.4% digitonin, 0.4% DM-NPG, 0.2% GDN101, and 0.2% LM-NPG (Anatrace) and incubated at 17°C for 1 hour. The extract was subsequently clarified by a high-speed centrifugation (60,000*g* for 1 hour), and the supernatant was subjected to a single-step IMAC purification. The $BcsB^{FL}$-bound resin was washed extensively with IMAC buffer A [20 mM Hepes (pH 8.0), 500 mM NaCl, 19 mM imidazole, and 0.008% LM-NPG] and eluted with buffer B containing 20 mM Hepes (pH 8.0), 500 mM NaCl, 0.008% LM-NPG, and 200 mM imidazole (pH 8.0). The quality of the eluted sample was verified by SDS-PAGE and used for cryo-EM grid preparation as described above.

SEC-coupled on-column cross-linking

To detect $BcsB^{FL}$ oligomerization in solution biochemically, we used SEC-coupled, on-column cross-linking (*13*). First, 200 µl of 0.25% glutaraldehyde was injected to a Superose 6 Increase 10/300 GL column (Cytiva), preequilibrated in buffer containing 20 mM Hepes (pH 8.0), 500 mM NaCl, 0.006% LM-NPG, and 0.006% GDN101. The run was stopped after 5 ml of elution volume, and the sample loop was flush-cleaned with the same buffer. Concentrated IMAC-purified full-length $BcsB^{His}$ was subsequently injected onto the column, and the run was continued. As the higher hydrodynamic radius of the protein sample incurs faster mobility through the chromatography column, protein assemblies passing through the glutaraldehyde bolus would be briefly exposed to the cross-linking agent and any nonspecific aggregates would be simultaneously separated by the gel filtration medium. The mild cross-linking of $BcsB^{FL}$ into higher–molecular weight species was visualized by running individual fractions across the non-aggregative elution peak on 4 to 20% SDS-PAGE gradient gels and Coomassie staining.

SDS-PAGE and Western blot analyses

Protein fractions were analyzed by standard denaturing SDS-PAGE electrophoresis using 4 to 20% gradient mini-gels (Bio-Rad), Expedeon InstantBlue Coomassie stain, and a Li-Cor Odyssey Fc system for Coomassie visualization (700-nm channel). For Western blot analyses, SDS-PAGE–migrated proteins were directly transferred using a standard mini-gel transfer protocol, polyvinylidene difluoride membranes, and a Trans-blot Turbo transfer system (Bio-Rad). Blocking and antibody incubations were performed in the presence of 5% skim milk in TPBS (1X phosphate-buffered saline supplemented with 0.1% Tween^{TM} 20 detergent); all washes between and after antibody incubations were performed with 1× TPBS buffer. Mouse anti-HA (hemagglutinin) (Thermo Fisher Scientific, #26183; dilution 1:1000) and anti-GAPDH (Thermo Fisher Scientific, #MA5-15738; dilution 1:1000) antibodies were used as primary antibodies; Alexa Fluor 680–conjugated donkey anti-mouse antibody (Abcam, ab175774; dilution 1:10,000) was used as secondary antibody. The signal was detected using a Li-Cor Odyssey Fc system in the 700-nm channel.

Crystallization, data collection, and structure determination

All crystals were obtained by sitting or hanging-drop vapor diffusion by mixing equal volumes of protein (1.5 to 6 mg/ml) and reservoir solution followed by incubation at 4°C. Crystallization conditions were as follows: Diffracting $BcsRQ^{His}$ crystals with P 1 21 1 space group appeared in multiple crystallization conditions with typical composition of 15 to 22% polyethylene glycol (PEG) 2000, 100 mM 2-(N-morpholino)ethanesulfonic acid (MES), or bis-tris with pH 5.5 to 6.5 and 0 to 7% glycerol or xylitol; $BcsRQ^{His}$ crystals with P 21 21 21 space group grew in 100 mM MES (pH 6.5) and 12% PEG 20,000; $BcsRQ^{R156E}$-$BcsE^{217–523}$ crystals appeared in 100 mM MES (pH 6.0) and 11% PEG 20,000; BcsRQ-$BcsE^{349–523}$ crystals grew in 100 mM Tris-HCl (pH 9.0), 22 to 25% PEG 6000, and 500 mM LiCl. For crystallization of AppCp- or ADP-pretreated $BcsRQ^{His}$, $MgCl_2$ and either nucleotide were also added to the crystallization condition at 500 and 50 µM final concentrations, respectively. For crystallization of $BcsE^{217–523}$ and the complexes $BcsRQ^{R156E}$-$BcsE^{217–523}$ and BcsRQ-$BcsE^{349–523}$, the crystallization conditions were supplemented with 50 µM c-di-GMP. All $BcsRQ^{His}$ crystals with P 1 21 1 space group, as well as all BcsE-containing crystals, appeared within 3 to 14 days, whereas $BcsRQ^{His}$ crystals with P 21 21 21 space group were detected 6 to 8 months after setting up of the crystallization trials. For cryo-protection, crystals were soaked in reservoir solution supplemented with 25 to 30% glycerol, 1 mM DTT, and, where applicable, 50 µM c-di-GMP. Cryo-preserved crystals were flash-frozen and stored in liquid nitrogen. Data were collected on frozen crystals at 100 K using synchrotron radiation at the European Synchrotron Radiation Facility (ESRF, beamline ID29 MX) and Soleil (beamlines PX1 and PX2) synchrotrons.

Data reduction was carried out with the software package XDS (*30*). Experimental phases were obtained by single-wavelength anomalous diffraction (SAD) experiments on crystals grown from selenomethionine-derivatized proteins and with wavelengths corresponding to the experimentally determined selenium K-edge. Initial models for the BcsRQ complex were built manually in the SAD-derived experimental density using Coot (*31*), and a BcsQ monomer was used as a search model in molecular replacement phasing of x-ray diffraction datasets collected on crystallized native complexes ($BcsRQ^{His}$, BcsRQ-$BcsE^{349–523}$, and $BcsRQ^{R156E}$-$BcsE^{217–523}$; tables S2 and S3). Models for the $BcsE^{GGDEF*}$ and Bcs^{REC*} domains were derived from the recently reported crystal structure of $BcsE^{217–523}$ (*10*) and used as additional search models in the molecular replacement phasing of the BcsRQ-$BcsE^{349–523}$ and $BcsRQ^{R156E}$-$BcsE^{217–523}$ datasets. Reiterative refinements in Phenix and Coot of all structures yielded the final refined models (*31*, *32*). Data collection and refinement statistics are summarized in tables S2 and S3. For illustration purposes, all crystal structures were displayed in the PyMOL Molecular Graphics System (Schrödinger LLC) or UCSF Chimera (*33*). The latter was also used for displaying the 3D reconstructions of the assembled Bcs macrocomplex.

Single-particle cryo-EM

To visualize the self-polymerization propensity of purified His-tagged $BcsB^{FL}$, we collected a dataset of 3830 movies on the Elsa Talos Arctica transmission electron microscope (Thermo Fisher Scientific) at the European Institute of Chemistry and Biology (IECB) Bordeaux operated at 200 kV and equipped with a Gatan K2 Summit direct electron detector. Movies of 67 frames were recorded using SerialEM (*34*) in electron counting mode at a total exposure dose of 49.6 $e^-/Å^2$ and a corrected pixel size of 1.13 $Å^2$. The movies were motion- and contrast transfer function (CTF)–corrected using MotionCor2 (*35*) and Gctf (*36*), respectively, within the cryoSPARC v2 interface. Particles were auto-picked using the latter's "blob picker" function, and after

three rounds of 2D classification in cryoSPARC v2 (*37*), a total of 46,807 particles distributed among 15 classes were retained and used in ab initio model generation and nonuniform refinement. Each $BcsB^{peri}$ octamer was further refined locally after subtraction of the remaining densities, and the resulting reconstructions were combined to yield the locally refined $BcsB^{peri}$ hexadecamer.

We used the same microscope to record a dataset of 6793 movies of the Bcs macrocomplex with similar data collection parameters (64 frames per movie, 48.3 $e^-/Å^2$ total exposure dose, corrected pixel size of 1.13 $Å^2$) and analysis workflow, yielding a final set of 286,771 particles distributed among 64 2D classes, the best of which were kept as templates for particle auto-picking in subsequent analyses (see below). For initial 3D model generation for the assembled Bcs macrocomplex, classes with less than five BcsB copies, as well as classes visually missing densities corresponding to the IM and/or cytosolic regions, were removed during the 2D classification. A 3D model was generated ab initio and subjected to nonuniform refinement; however, the overall resolution of the IM and cytosolic modules was not sufficiently high for reliable density assignment.

To further resolve the 3D architecture of the assembled Bcs macrocomplex, we therefore recorded a total of 9129 movies on the CM01 Titan Krios transmission electron microscope (Thermo Fisher Scientific) at the ESRF Grenoble operated at 300 kV and equipped with a Gatan K2 Summit direct electron detector and a GIF Quantum LS imaging filter (*38*). The images were collected in two separate sessions keeping a constant total electron dose (48 $e^-/Å^2$), defocus range (−0.75 to −2.75 μm), and pixel size (1.05248 $Å^2$). The movies were motion- and CTF-corrected as above, using MotionCor2 and Gctf within the cryoSPARC v2 interface (*35*–*37*). Particles were autopicked using the cryoSPARC v2 template picker and 2D classes generated from the initial Talos Arctica dataset. The resulting particle stacks from each dataset were then subjected to three rounds of 2D classification for removal of "junk" particles. A total of 576,455 particles containing three to six identifiable BcsB copies were then used for ab initio model generation using a single class. Nonuniform refinement of the resultant model yielded a 3D reconstruction corresponding to a BcsB pentamer resolved at ~3.1-Å average resolution accompanied by lower-intensity, lower-resolution regions corresponding to the rest of the Bcs macrocomplex. The map was segmented in UCSF Chimera (*33*) and separate soft masks for the BcsB pentamer, and the rest of the assembly were generated in cryoSPARC v2 (*37*). The low-resolution regions were then subtracted from the refined particles, and the BcsB pentamer was locally refined to 2.9-Å average resolution, with extensive regions featuring local resolution at 2.5 Å. The nonuniformly refined maps before and after local refinement were then autosharpened and combined in Phenix (*32*). Initial BcsB backbone tracing and atomic model building were performed manually for a single BcsB subunit in Coot (*31*). The model was then used for generation of a BcsB pentamer, which was thoroughly refined against the experimental density map through iterative model building and refinement cycles in Coot and Phenix, respectively. Coordinate refinement statistics are summarized in table S1.

To improve the resolution of the BcsRQAB assembly (fig. S7), we first removed a substantial part of the partially assembled Bcs complexes by force-splitting the dataset through 3D classification between two classes: a BcsB crown pentamer and an assembled Bcs macrocomplex as derived from the model generated from the Talos Arctica dataset. The latter class was then subjected to nonuniform refinement in cryoSPARC v2 and two rounds of 3D variability analysis and display in clusters (*37*), where only particles belonging to clusters with resolved IM and cytosolic densities were retained for further analysis. A resulting stack of 173,294 particles were then input for ab initio model generation and nonuniform refinement, and the resulting 3D density reconstruction was segmented in UCSF Chimera (*33*). Separate soft masks were generated for the BcsRQAB assembly (i.e., regions corresponding to the apical $BcsR_2Q_2$ complex; to BcsA's TMD, GT, and PilZ domains; and to the partner BcsB copy) and the rest of the reconstruction. The latter mask was used as input for particle subtraction, and the remaining BcsRQAB assembly was locally refined. A BcsA homology model was generated in Robetta (*15*) based on the $BcsA^{R.sphaeroides}$ crystal structures, and its separate domains were rigid body–fitted and refined against the locally refined BcsRQAB-corresponding cryo-EM density.

Isothermal titration calorimetry

Apparent dissociation constants (K_d) and stoichiometry of interactions (N) were measured by isothermal titration calorimetry (ITC) (*39*) using a Microcal VP-ITC calorimeter from Malvern Panalytical at 20°C. For c-di-GMP binding studies, 0.8 to 1 mM c-di-GMP were used as a ligand in the syringe and purified protein was added to the cuvette at concentrations of 40 to 50 μM. The protein and ligand were purified/diluted in the exact same buffer to minimize nonspecific dilution heat effects. Protein concentrations were determined by a combination of methods including a reducing agent–compatible colorimetric assay (RC DC, Bio-Rad) and 280-nm absorbance measurements under denaturing conditions (A_{280}; 6 M guanidinium chloride) while accounting for potential scattering contributions (A_{330}). All ITC data were analyzed by integrating the injection heat effects, normalized to the amount of ligand and protein present, and curve-fitting based on a single- or two-site binding models using the Origin software package for Microcal. For all titrations, titrations of the ligand into buffer were performed to account for heat dilution effects, and the latter were subtracted during the ligand binding analyses. The apparent K_d and N were derived from the data by using standard procedures, and the graphs were replotted using the GraphPad Prism software.

Calcofluor-binding cellulose secretion assay

To test for the functional effects of BcsQ and BcsR point mutants or truncated variants, we resorted to a functional complementation assay as established previously (*4*). First, chemically competent cells were prepared from *E. coli* 1094 Δ*bcsQ* or Δ*bcsR* deletion strains (*4*). These were then transformed with low-copy pAM-238 plasmids carrying wild-type or mutant *bcsQ* or *bcsR* genes and plated on LB-agar plates (Miller) supplemented with the appropriate antibiotics [streptomycin (60 μg/ml) and chloramphenicol (15 μg/ml)]. Single colonies were inoculated in 5 ml of LB medium with antibiotics and left to grow overnight at 37°C and agitation. On the following morning, 5 μl of the cultures was spotted onto low-salt LB-agar plates [NaCl (1.5 g/liter)] supplemented with the antibiotics, 0.1 mM IPTG, and 0.02% calcofluor (Fluorescent Brightener 28, Sigma-Aldrich). The spots were allowed to air-dry, and the plates were incubated at 30°C. After 24 hours, the plates were photographed under brief illumination with long-wave ultraviolet light (365 nm).

Nucleotide loading state analysis

We used reversed-phase high-performance liquid chromatography to separate nucleotides for the determination of nucleotide loading

states of purified protein complexes. Purified wild-type and mutant BcsRQ complexes were purified by IMAC and gel filtration as described above and concentrated to 20 mg/ml using Microcon Centrifugal Filter units (Merck Millipore) with a 10-kDa cutoff. The concentrated protein samples were denatured on ice using equal volume of chilled isopropanol and immediately resuspended with water to 40 μM final protein concentration. Each sample was subsequently filtered through Microcon Centrifugal Filter units (Millipore) with a 10-kDa cutoff, and nucleotides were separated on a C18 reversed-phase column (Poroshell 120 EC-C18 3 × 150 mm, 2.7 μm, flow rate of 0.5 ml/min) using 100 mM potassium phosphate buffer (buffer A, pH 6.0) as mobile phase (6 min), followed by a methanol-phosphate gradient for column cleanup and reequilibration [1 min 0 to 100% buffer B (30% methanol/70% buffer A), 4 min 100% buffer B, 1 min 100 to 0% buffer B, 2 min buffer A]. Eluted nucleotides were identified by comparison to injected ATP and ADP standards.

ATP hydrolysis assay

ATPase activity assays were conducted using the ATPase/GTPase activity kit (MAK113, Sigma-Aldrich) according to the manufacturer's guidelines. Following IMAC and SEC purification, wild-type and mutant BcsRQ complexes were diluted to final concentrations of 5, 2.5, 1.25, and 0.625 μM in gel filtration buffer [20 mM Hepes (pH 8.0), 120 mM NaCl, and 2 mM DTT]. Ten microliters of each sample was mixed with 20 μl of the provided assay buffer [40 mM tris-HCl (pH 7.5), 80 mM NaCl, 8 mM $MgAc_2$, and 1 mM EDTA] and 10 μl of 4 mM freshly prepared ATP in a microplate. The reactions were incubated for 25 min at room temperature before stopping them by the addition of the malachite green–containing blocking reagent. The samples were left to develop for additional 25 min at room temperature to allow the malachite green to form a stable dark green product with the free phosphate liberated by the ATPase reactions. The colorimetric products, proportional to enzyme activity, were measured in a microplate reader at 620 nm. A previously characterized active ATPase [$FleQ^{T149E}$ (*40*)] was used as a positive control, and negative control wells contained gel filtration buffer in lieu of protein sample.

SUPPLEMENTARY MATERIALS

Supplementary material for this article is available at http://advances.sciencemag.org/cgi/content/full/7/5/eabd8049/DC1

View/request a protocol for this paper from *Bio-protocol*.

REFERENCES AND NOTES

1. U. Römling, M. Y. Galperin, Bacterial cellulose biosynthesis: Diversity of operons, subunits, products, and functions. *Trends Microbiol.* **23**, 545–557 (2015).
2. E. Petersen, E. Mills, S. I. Miller, Cyclic-di-GMP regulation promotes survival of a slow-replicating subpopulation of intracellular *Salmonella* Typhimurium. *Proc. Natl. Acad. Sci. U.S.A.* **116**, 6335–6340 (2019).
3. E. Rossi, A. Cimdins, P. Lüthje, A. Brauner, Å. Sjöling, P. Landini, U. Römling, "It's a gut feeling"—*Escherichia coli* biofilm formation in the gastrointestinal tract environment. *Crit. Rev. Microbiol.* **44**, 1–30 (2017).
4. P. V. Krasteva, J. Bernal-Bayard, L. Travier, F. A. Martin, P.-A. Kaminski, G. Karimova, R. Fronzes, J.-M. Ghigo, Insights into the structure and assembly of a bacterial cellulose secretion system. *Nat. Commun.* **8**, 2065 (2017).
5. J. L. W. Morgan, J. T. McNamara, J. Zimmer, Mechanism of activation of bacterial cellulose synthase by cyclic di-GMP. *Nat. Struct. Mol. Biol.* **21**, 489–496 (2014).
6. J. L. W. Morgan, J. Strumillo, J. Zimmer, Crystallographic snapshot of cellulose synthesis and membrane translocation. *Nature* **493**, 181–186 (2013).
7. J. L. W. Morgan, J. T. McNamara, M. Fischer, J. Rich, H.-M. Chen, S. G. Withers, J. Zimmer, Observing cellulose biosynthesis and membrane translocation *in crystallo*. *Nature* **531**, 329–334 (2016).
8. O. Omadjela, A. Narahari, J. Strumillo, H. Mélida, O. Mazur, V. Bulone, J. Zimmer, BcsA and BcsB form the catalytically active core of bacterial cellulose synthase sufficient for in vitro cellulose synthesis. *Proc. Natl. Acad. Sci. U.S.A.* **110**, 17856–17861 (2013).
9. W. Thongsomboon, D. O. Serra, A. Possling, C. Hadjineophytou, R. Hengge, L. Cegelski, Phosphoethanolamine cellulose: A naturally produced chemically modified cellulose. *Science* **359**, 334–338 (2018).
10. S. Zouhir, W. Abidi, M. Caleechurn, P. V. Krasteva, Structure and multitasking of the c-di-GMP-sensing cellulose secretion regulator BcsE. *MBio* **11**, e01303-20 (2020).
11. B. Le Quéré, J.-M. Ghigo, BcsQ is an essential component of the *Escherichia coli* cellulose biosynthesis apparatus that localizes at the bacterial cell pole. *Mol. Microbiol.* **72**, 724–740 (2009).
12. T. R. D. Costa, C. Felisberto-Rodrigues, A. Meir, M. S. Prevost, A. Redzej, M. Trokter, G. Waksman, Secretion systems in Gram-negative bacteria: Structural and mechanistic insights. *Nat. Rev. Microbiol.* **13**, 343–359 (2015).
13. A. K. Shukla, G. H. Westfield, K. Xiao, R. I. Reis, L.-Y. Huang, P. Tripathi-Shukla, J. Qian, S. Li, A. Blanc, A. N. Oleskie, A. M. Dosey, M. Su, C.-R. Liang, L.-L. Gu, J.-M. Shan, X. Chen, R. Hanna, M. Choi, X. J. Yao, B. U. Klink, A. W. Kahsai, S. S. Sidhu, S. Koide, P. A. Penczek, A. A. Kossiakoff, V. L. Woods Jr., B. K. Kobilka, G. Skiniotis, R. J. Lefkowitz, Visualization of arrestin recruitment by a G-protein-coupled receptor. *Nature* **512**, 218–222 (2014).
14. H. P. Chen, R. M. Brown Jr., Immunochemical studies of the cellulose synthase complex in *Acetobacter xylinum*. *Cellulose* **3**, 63–75 (1996).
15. D. E. Kim, D. Chivian, D. Baker, Protein structure prediction and analysis using the Robetta server. *Nucleic Acids Res.* **32**, W526–W531 (2004).
16. G. Bange, I. Sinning, SIMIBI twins in protein targeting and localization. *Nat. Struct. Mol. Biol.* **20**, 776–780 (2013).
17. S.-O. Shan, ATPase and GTPase tangos drive intracellular protein transport. *Trends Biochem. Sci.* **41**, 1050–1060 (2016).
18. I. Hayashi, T. Oyama, K. Morikawa, Structural and functional studies of MinD ATPase: Implications for the molecular recognition of the bacterial cell division apparatus. *EMBO J.* **20**, 1819–1828 (2001).
19. J. L. Bos, H. Rehmann, A. Wittinghofer, GEFs and GAPs: Critical elements in the control of small G proteins. *Cell* **129**, 865–877 (2007).
20. K. T. Park, W. Wu, K. P. Battaile, S. Lovell, T. Holyoak, J. Lutkenhaus, The Min oscillator uses MinD-dependent conformational changes in MinE to spatially regulate cytokinesis. *Cell* **146**, 396–407 (2011).
21. K.-T. Park, W. Wu, S. Lovell, J. Lutkenhaus, Mechanism of the asymmetric activation of the MinD ATPase by MinE. *Mol. Microbiol.* **85**, 271–281 (2012).
22. T. A. Leonard, P. J. Butler, J. Löwe, Bacterial chromosome segregation: Structure and DNA binding of the Soj dimer––A conserved biological switch. *EMBO J.* **24**, 270–282 (2005).
23. G. Bange, N. Kümmerer, P. Grudnik, R. Lindner, G. Petzold, D. Kressler, E. Hurt, K. Wild, I. Sinning, Structural basis for the molecular evolution of SRP-GTPase activation by protein. *Nat. Struct. Mol. Biol.* **18**, 1376–1380 (2011).
24. S. Stefer, S. Reitz, F. Wang, K. Wild, Y.-Y. Pang, D. Schwarz, J. Bomke, C. Hein, F. Löhr, F. Bernhard, V. Denic, V. Dötsch, I. Sinning, Structural basis for tail-anchored membrane protein biogenesis by the Get3-receptor complex. *Science* **333**, 758–762 (2011).
25. P. V. Krasteva, J. C. N. Fong, N. J. Shikuma, S. Beyhan, M. V. A. S. Navarro, F. H. Yildiz, H. Sondermann, *Vibrio cholerae* VpsT regulates matrix production and motility by directly sensing cyclic di-GMP. *Science* **327**, 866–868 (2010).
26. J. Nesper, I. Hug, S. Kato, C.-S. Hee, J. M. Habazettl, P. Manfredi, S. Grzesiek, T. Schirmer, T. Emonet, U. Jenal, Cyclic di-GMP differentially tunes a bacterial flagellar motor through a novel class of CheY-like regulators. *eLife* **6**, e28842 (2017).
27. P. Ross, H. Weinhouse, Y. Aloni, D. Michaeli, P. Weinberger-Ohana, R. Mayer, S. Braun, E. de Vroom, G. A. van der Marel, J. H. van Boom, M. Benziman, Regulation of cellulose synthesis in *Acetobacter xylinum* by cyclic diguanylic acid. *Nature* **325**, 279–281 (1987).
28. S. Kimura, H. P. Chen, I. M. Saxena, R. M. Brown Jr., T. Itoh, Localization of c-di-GMP-binding protein with the linear terminal complexes of *Acetobacter xylinum*. *J. Bacteriol.* **183**, 5668–5674 (2001).
29. A. M. Richter, A. Possling, N. Malysheva, K. P. Yousef, S. Herbst, M. Kleist, R. Hengge, Local c-di-GMP signaling in the control of synthesis of the *E. coli* biofilm exopolysaccharide pEtN-cellulose. *J. Mol. Biol.* **432**, 4576–4595 (2020).
30. W. Kabsch, XDS. *Acta Crystallogr. D Biol. Crystallogr.* **66**, 125–132 (2010).
31. P. Emsley, B. Lohkamp, W. G. Scott, K. Cowtan, Features and development of Coot. *Acta Crystallogr. D Biol. Crystallogr.* **66**, 486–501 (2010).
32. P. D. Adams, P. V. Afonine, G. Bunkóczi, V. B. Chen, I. W. Davis, N. Echols, J. J. Headd, L.-W. Hung, G. J. Kapral, R. W. Grosse-Kunstleve, A. J. McCoy, N. W. Moriarty, R. Oeffner, R. J. Read, D. C. Richardson, J. S. Richardson, T. C. Terwilliger, P. H. Zwart, *PHENIX*: A comprehensive Python-based system for macromolecular structure solution. *Acta Crystallogr. D Biol. Crystallogr.* **66**, 213–221 (2010).
33. E. F. Pettersen, T. D. Goddard, C. C. Huang, G. S. Couch, D. M. Greenblatt, E. C. Meng, T. E. Ferrin, UCSF Chimera––A visualization system for exploratory research and analysis. *J. Comput. Chem.* **25**, 1605–1612 (2004).

34. D. N. Mastronarde, Automated electron microscope tomography using robust prediction of specimen movements. *J. Struct. Biol.* **152**, 36–51 (2005).
35. S. Q. Zheng, E. Palovcak, J.-P. Armache, K. A. Verba, Y. Cheng, D. A. Agard, MotionCor2: Anisotropic correction of beam-induced motion for improved cryo-electron microscopy. *Nat. Methods* **14**, 331–332 (2017).
36. K. Zhang, Gctf: Real-time CTF determination and correction. *J. Struct. Biol.* **193**, 1–12 (2016).
37. A. Punjani, J. L. Rubinstein, D. J. Fleet, M. A. Brubaker, cryoSPARC: Algorithms for rapid unsupervised cryo-EM structure determination. *Nat. Methods* **14**, 290–296 (2017).
38. E. Kandiah, T. Giraud, A. de Maria Antolinos, F. Dobias, G. Effantin, D. Flot, M. Hons, G. Schoehn, J. Susini, O. Svensson, G. A. Leonard, C. Mueller-Dieckmann, CM01: A facility for cryo-electron microscopy at the European Synchrotron. *Acta Crystallogr. D Struct. Biol.* **75**, 528–535 (2019).
39. B. Y. Matsuyama, P. V. Krasteva, M. V. A. S. Navarro, Isothermal titration calorimetry to determine apparent dissociation constants (K_d) and stoichiometry of interaction (n) of C-di-GMP binding proteins. *Methods Mol. Biol.* **1657**, 403–416 (2017).
40. B. Y. Matsuyama, P. V. Krasteva, C. Baraquet, C. S. Harwood, H. Sondermann, M. V. A. S. Navarro, Mechanistic insights into c-di-GMP-dependent control of the biofilm regulator FleQ from *Pseudomonas aeruginosa*. *Proc. Natl. Acad. Sci. U.S.A.* **113**, E209–E218 (2016).

Acknowledgments: We are grateful to all current and former members of the SBB group and especially to A. Thomas-Collignon, M. Poulain, G. Shajepal, and L. Torres-Sanchez for technical assistance and/or work peripheral to the project; to the I2BC Virology department for provided equipment and lab space; to Y. Yamaichi, V. Lioy, J. M. Ghigo, S. Létoffé, J. Bernal-Bayard, and H. Sondermann for providing expression vectors and bacterial strains; to members of the Reyes, Innis, Fronzes, and Hashem laboratories for discussions; and to A. Bezault, E. Kandiah, C. Dian, and the beamline scientists at Soleil for data collection assistance. **Funding:** This project received funding from the ERC Executive Agency under grant agreement 757507—BioMatrix-ERC-2017-StG (to P.V.K.) and was also supported by the I2BC, the IECB, the CNRS, an ATIP-Avenir grant (to P.V.K.), and a Université de Bordeaux IDEX Junior Chair grant (to P.V.K.). The work has also benefited from the I2BC platforms PIM and cryo-EM, which are supported by FRISBI (ANR-10-INBS-05), the IECB cryo-EM platform and Elsa the Talos Arctica, the Soleil synchrotron, and the ERSF. **Author contributions:** P.V.K. conceived the project. P.V.K., W.A., S.Z., and M.C. designed, performed, and optimized the experimental procedures. P.V.K., S.Z., and W.A. analyzed the data. S.R. contributed to the crystallographic data processing and with useful discussions, and P.V.K. wrote the paper with feedback from coauthors. **Competing interests:** The authors declare that they have no competing interests. **Data and materials availability:** All data needed to evaluate the conclusions in the paper are present in the paper and/or the Supplementary Materials. Refined structural models and electron density maps have been deposited in the electron microscopy and protein databanks. Assigned accession codes are as follows: emd-10799 and pdb-6yg8 for the $BcsB^{peri}$ pentamer; emd-11356 for the $BcsB^{FL}$ hexadecamer; emd-11836 for the BcsRQAB assembly and Bcs macrocomplex; pdb-codes 6yar, 6yay, 6yb3, and 6yb5 for the $BcsRQ^{His}$ complexes; pdb-6ybu for the $BcsRQE^{349-523}$ complex; and pdb-6ybb for the $BcsRQ^{R156E}E^{217-523}$ complex. Additional requests may be addressed to the corresponding author.

Submitted 13 July 2020
Accepted 8 December 2020
Published 27 January 2021
10.1126/sciadv.abd8049

Citation: W. Abidi, S. Zouhir, M. Caleechurn, S. Roche, P. V. Krasteva, Architecture and regulation of an enterobacterial cellulose secretion system. *Sci. Adv.* **7**, eabd8049 (2021).

Science Advances

Architecture and regulation of an enterobacterial cellulose secretion system

Wiem Abidi, Samira Zouhir, Meryem Caleechurn, Stéphane Roche and Petya Violinova Krasteva

Sci Adv **7** (5), eabd8049.
DOI: 10.1126/sciadv.abd8049

Science Advances
AAAS

advances.sciencemag.org/cgi/content/full/7/5/eabd8049/DC1

Supplementary Materials for

Architecture and regulation of an enterobacterial cellulose secretion system

Wiem Abidi, Samira Zouhir, Meryem Caleechurn, Stéphane Roche, Petya Violinova Krasteva*

*Corresponding author. Email: pv.krasteva@iecb.u-bordeaux.fr

Published 27 January 2021, *Sci. Adv.* **7**, eabd8049 (2021)
DOI: 10.1126/sciadv.abd8049

This PDF file includes:

Figure S1. Quaternary structure of BcsB$^{E.coli}$. (**A**) Views of a refined BcsB$^{E.coli}$ pentamer against the experimental cryo-EM density following local refinement within the assembled Bcs macrocomplex. (**B**) Surface map coloring according to FSC-based local resolution estimations, color key in angstroms. (**C**) FSC plots and average resolution estimations for the locally refined BcsB pentamer at the gold-standard FSC cutoff of 0.143. Cryo-EM data analysis was carried out in cryoSPARC v2, atomic model building and refinement in Phenix, map visualization in UCSF Chimera. (**D**) A modeled decameric BcsB$^{E.coli}$ superhelix based on the experimentally observed inter-subunit contacts presented in (**A**). The stacked luminal loops are shown in surface representation, the rest of each BcsB subunit is shown as cartoon. Calculations of the rotational and translational displacements between the first and last protomer, as well as structure visualization were carried out in PyMol. (**E**) Elution profile of purified full-length BcsB^{His} subjected to size-exclusion chromatography (SEC) coupled with non-aggregative, on-column crosslinking. SEC column: Superose® 6 Increase 10/300 GL (Cytiva). (**F**) SDS-PAGE analysis of the IMAC elution fraction of purified full-length BcsB^{His} (lane 2) and the SEC-elution fractions of the same sample following mild on-column crosslinking and gel filtration, as in (**E**). (**G**) Comparison of BcsB^{peri} packing observed in the structure of IMAC-purified full-length BcsB^{His} (rainbow, one of two experimentally observed octamers presented) vs. BcsB^{peri} packing as observed in the Bcs macrocomplex crown (grey, an octamer model based on inter-subunit contacts presented in (**A**)). The two octamers were aligned onto the first BcsB copy, calculations of the rotational and translational displacements between the last protomers of each assembly were carried out in PyMol.

Figure S2. Sequence and structure comparison of BcsB$^{E.coli}$ and BcsB$^{R.sphaeroides}$. (**A**) Fold comparison of the four periplasmic BcsB domains with emphasis on key motifs participating in inter-subunit β-strand-mediated backbone interactions. (**B**) Sequence and secondary structure alignment of the two homologs based on a published crystal structure of *R. sphaeroides* (pdb code: 4p00) and the cryo-EM data presented here. (**C**) A close-up view of the sequence-independent inter-subunit β-sheet complementation. (**D**) Sequence alignment of the key interface β-strand regions among enterobacteria. (**E**) Corresponding consensus logos and secondary structure predictions. Fold comparison was visualized in PyMol. Sequence alignments were performed in ClustalΩ and visualized in Jalview. Secondary structure prediction was carried out on the full-length enterobacterial BcsB consensus sequence in JPred. Consensus logos were generated in WebLogo.

Figure S3. Structure-function analyses of the BcsRQ complex. (**A**) Secondary structure topology of the BcsR (grey gradient) and BcsQ (rainbow) subunits. (**B**) Interface analysis of the BcsRQ complex. Surface areas and free energy gains were calculated in PDBePISA. (**C**) Close-up views of the BcsR:BcsQ interface. (**D**) Pre-catalytic nucleotide-bound 'tango' dimers of diverse SIMIBI proteins and their cellular functions. (**E**) SDS-PAGE analysis of IMAC elution fractions of Bcs^{His}RQ*-BcsE$^{217-523}$ complexes with BcsQ mutants presented in this study. (**F**) SEC elution

profiles and SDS-PAGE analysis of the elution peaks for BcsRQ* complexes containing a subset of BcsQ variants showing significant phenotypic effects on cellulose secretion. The $BcsQ^{R156E-N152D}$ mutant was unstable following IMAC elution and did not yield stable BcsRQ complex upon gel filtration. (**G**) ATPase activity of the purified BcsRQ* complexes visualized by a colorimetric malachite green-based assay (MAK113, Sigma-Aldrich). The active ATPase $FleQ^{T149E}$ was used as a positive control. (**H**) Nucleotide loading states of purified BcsRQ* complexes as detected by protein complex concentration, protein precipitation and reversed-phase HPLC analysis of the liberated nucleotides. Elution times of stably bound nucleotides concentrated together with the protein complexes are compared to those of individually injected ADP and ATP standards. (**I**) SEC-elution and ATPase activity profiles of purified $Bcs^{His}RQ^{WT}$-$BcsE^{217-523}$ and $Bcs^{His}RQ^{R156E}$-$BcsE^{217-523}$ heterocomplexes. Left: representative gel filtration profiles on a Superdex® 200 Increase 10/300 GL column (Cytiva). SEC buffer: 120 mM NaCl, 20 mM HEPES pH 8.0 and 2 mM DTT. Right: ATPase activity visualized as in (**G**).

Figure S4. Sequence alignments of enterobacterial cellulose secretion regulators. Alignments of representative BcsQ (**A**), BcsR (**B**) and BcsE (**C**) homologs with key residues, sequence motifs, secondary structure elements and domain organization as identified. Blue color intensity/darkness correlates with sequence conservation. The sequence alignment was generated in ClustalΩ and visualized with Jalview.

Figure S5. Surface conservation mapping of Bcs subunits and assemblies. Left, surface representation (PyMol) with domain color-coding as in the rest of the manuscript. Right, surface conservation presented as cyan (0%) – maroon (100%) gradients (UCSF Chimera).

Figure S6. BcsE-BcsQ interactions and crystal structure of the BcsRQ-$BcsE^{GGDEF*}$ complex. (**A**) Crystal structure of the BcsRQ-$BcsE^{349-523}$ complex. BcsQ is colored in green and blue, BcsR in pink and yellow, the GGDEF* domain in dark red, the I-site in cyan, the interstitial helix in tan, and C-terminal BcsE tail ($BcsE^{CT}$) in purple. ATP and c-di-GMP are shown as sticks, Mg^{++} ions as spheres. (**B**) Close-up views of the interface between the $BcsE^{GGDEF*}$ domain and the C-proximal BcsQ region. (**C**) A close-up view of the $BcsE^{CT}$: BcsQ interface. Interface BcsE residues are indicated on the left, BcsQ residues on the right. (**D**) Structural motifs in the $BcsE^{349-523}$ construct and interface analysis of the binary BcsE : BcsQ interaction as calculated in PDBePISA. (**E**) Dependence of BcsE-BcsQ complex formation on both the $BcsE^{GGDEF*}$ and $BcsE^{CT}$ components. (**F**) Head-to-head crystallographic packing of the BcsRQ-$BcsE^{349-523}$ complex. (**G**) C-di-GMP coordination in the BcsRQ$E^{349-523}$: c-di-GMP crystals. Left, an (|Fo|-|Fc|) partial electron density map calculated from a model prior to inclusion of the dinucleotide and contoured at 3σ. Right, I-site bound c-di-GMP coordination by BcsE, BcsR, and BcsQ residues from a symmetry related complex. (**H-I**) Summary of c-di-GMP coordinating motifs observed in this study as mapped onto the BcsE domain architecture (**H**) and a composite BcsRQ$E^{REC*-GGDEF*}$ assembly featuring a 'splayed' $BcsE^{217-523}$ module (**I**).

Figure S7. Cryo-EM data analysis workflow for the BcsRQAB complex. (**A**) Particle curation strategy for BcsRQAB focused refinement within the assembled Bcs macrocomplex. (**B**) Surface coloring of the unsharpened BcsRQAB reconstruction according to FSC-based local resolution estimations, color key in angstroms. (**C**) FSC plots and average resolution estimations for the locally refined BcsRQAB assembly at the gold-standard FSC cutoff of 0.143. (**D**) A snapshot of the modeled BcsA and BcsB transmembrane regions as fitted in the experimental electron density.

Table S1. Cryo-EM data collection and refinement statistics for the BcsB pentamer

Table S2. Crystallographic data collection and refinement statistics for the BcsRQ complexes

Table S3. Crystallographic data collection and refinement statistics for the BcsRQE* complexes

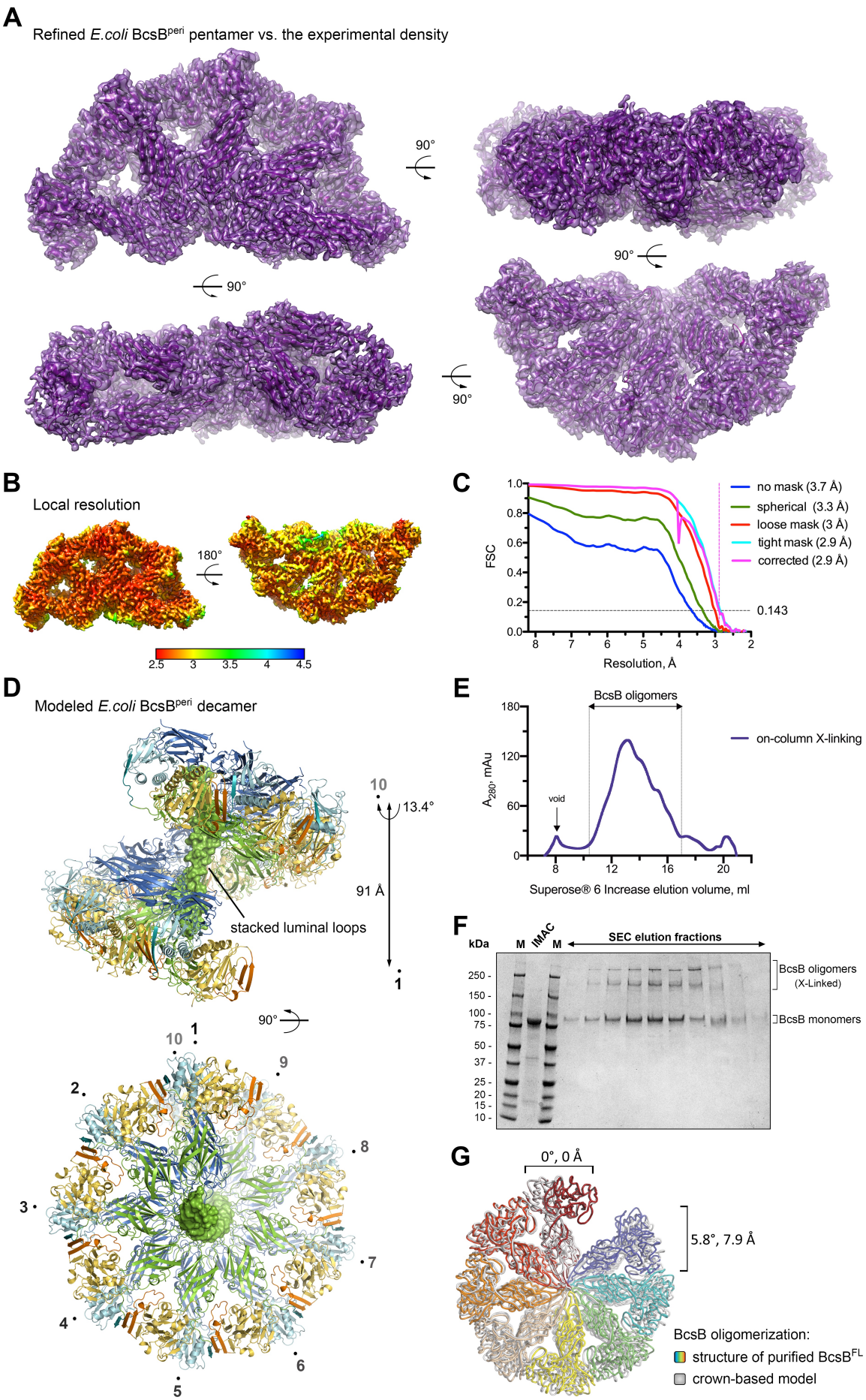
A
Refined E.coli BcsB^peri pentamer vs. the experimental density
90°
90°
90°
90°
B
Local resolution
180°
2.5
3
3.5
4
4.5
C
FSC
1.0
0.8
0.6
0.4
0.2
0.0
8
7
6
5
4
3
2
Resolution, Å
no mask (3.7 Å)
spherical (3.3 Å)
loose mask (3 Å)
tight mask (2.9 Å)
corrected (2.9 Å)
0.143
D
Modeled E.coli BcsB^peri decamer
10
13.4°
91 Å
1
stacked luminal loops
90°
10
1
9
2
8
3
7
4
6
5
E
BcsB oligomers
180
120
60
0
A280, mAu
void
8
12
16
20
Superose® 6 Increase elution volume, ml
on-column X-linking
F
kDa
M
IMAC
M
SEC elution fractions
250 -
150 -
100 -
75 -
50 -
37 -
25 -
20 -
15 -
10 -
BcsB oligomers
(X-Linked)
BcsB monomers
G
0°, 0 Å
5.8°, 7.9 Å
BcsB oligomerization:
structure of purified BcsB^FL
crown-based model

Figure S1

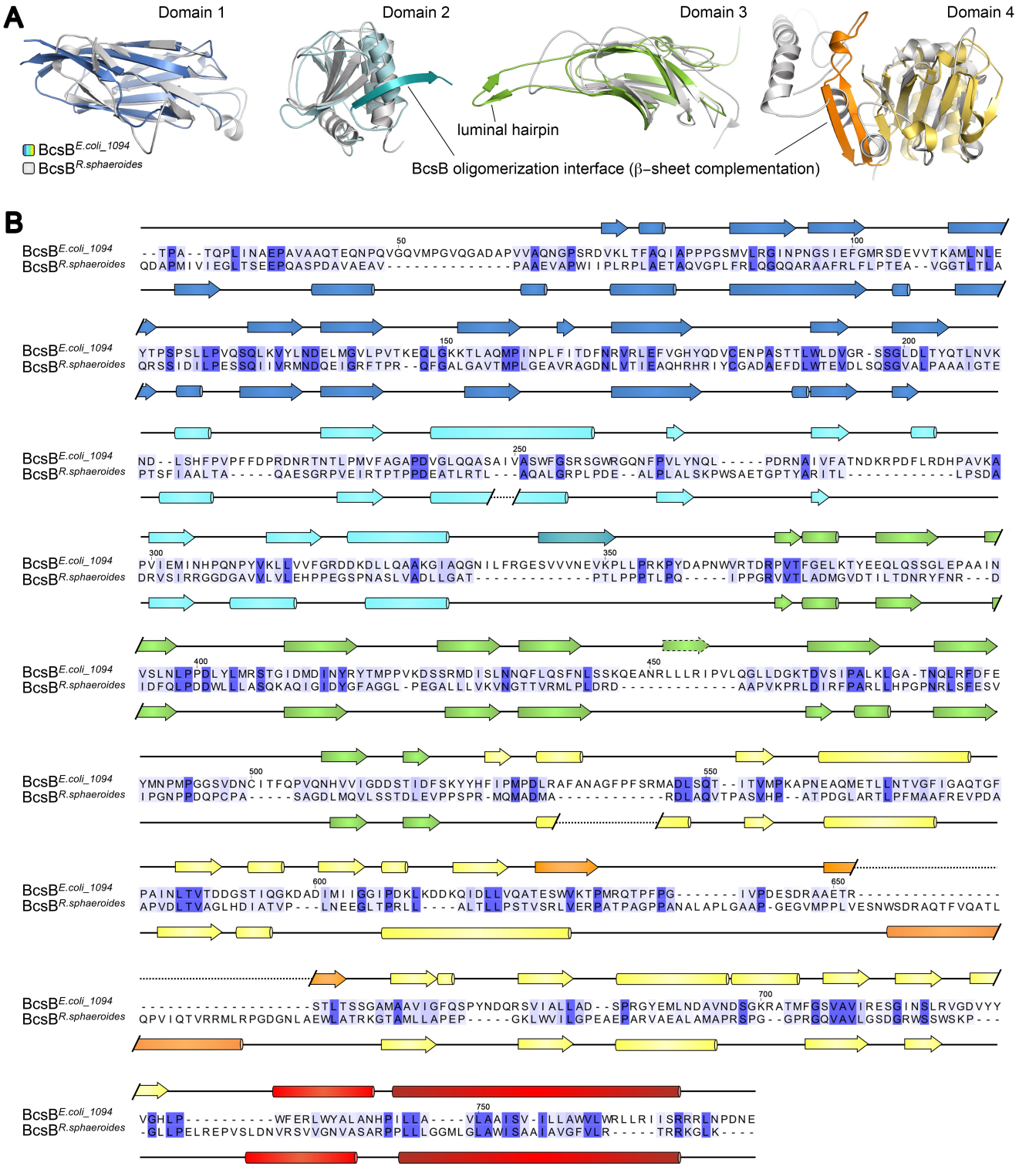
A
Domain 1
Domain 2
Domain 3
Domain 4
BcsB E.coli_1094
BcsB R.sphaeroides
luminal hairpin
BcsB oligomerization interface (β–sheet complementation)
B
BcsB E.coli_1094
BcsB R.sphaeroides
C
D
E

Figure S2

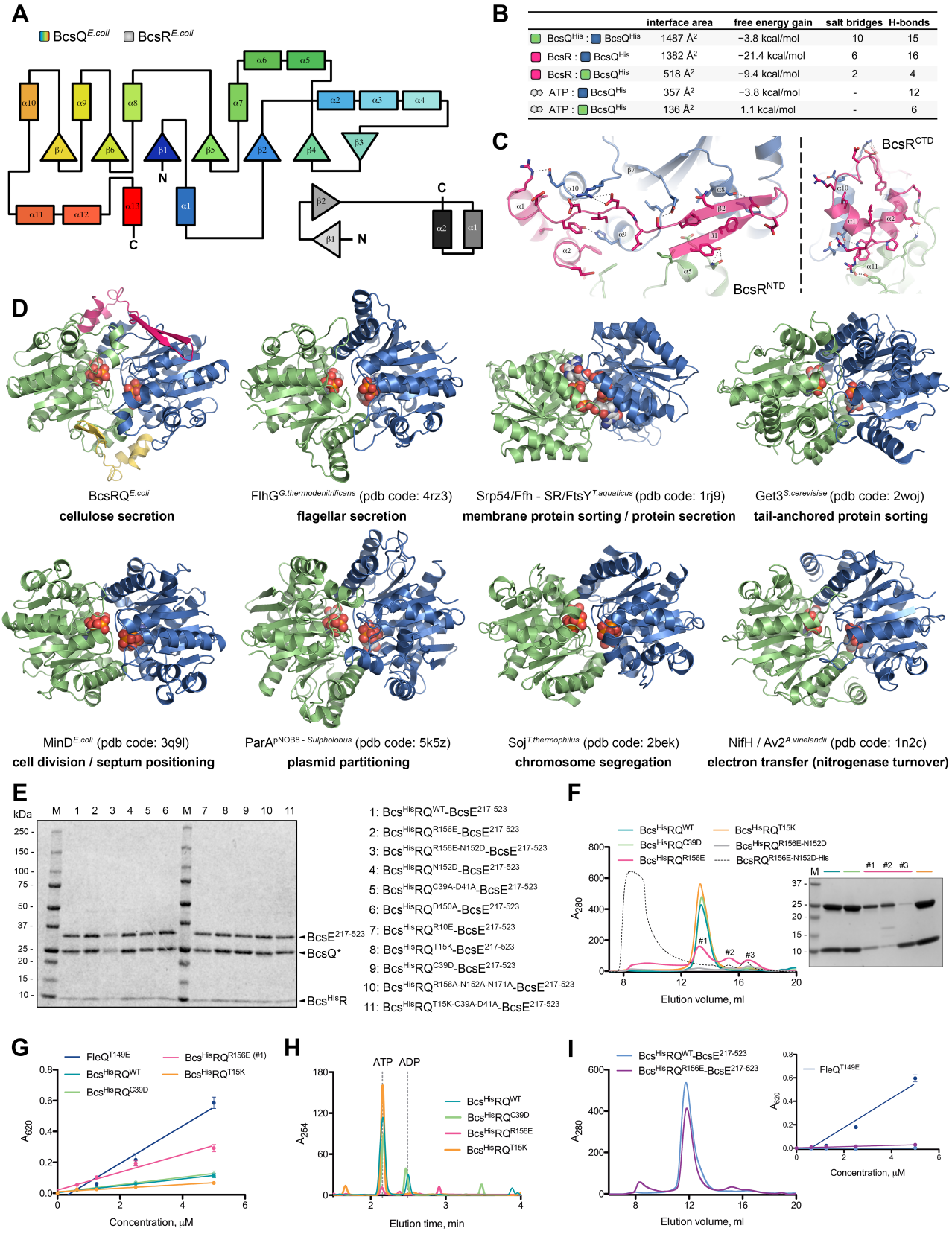
A
BcsQ E.coli
BcsR E.coli
α10
α9
α8
α7
α6
α5
α4
α3
α2
β7
β6
β1
β5
β2
β4
β3
N
α11
α12
α13
α1
C
β2
β1
N
C
α2
α1
B
interface area
free energy gain
salt bridges
H-bonds
BcsQHis : BcsQHis
1487 Å2
−3.8 kcal/mol
10
15
BcsR : BcsQHis
1382 Å2
−21.4 kcal/mol
6
16
BcsR : BcsQHis
518 Å2
−9.4 kcal/mol
2
4
ATP : BcsQHis
357 Å2
−3.8 kcal/mol
-
12
ATP : BcsQHis
136 Å2
1.1 kcal/mol
-
6
C
BcsRCTD
BcsRNTD
D
BcsRQE.coli
cellulose secretion
FlhGG.thermodenitrificans (pdb code: 4rz3)
flagellar secretion
Srp54/Ffh - SR/FtsYT.aquaticus (pdb code: 1rj9)
membrane protein sorting / protein secretion
Get3S.cerevisiae (pdb code: 2woj)
tail-anchored protein sorting
MinDE.coli (pdb code: 3q9l)
cell division / septum positioning
ParApNOB8 - Sulpholobus (pdb code: 5k5z)
plasmid partitioning
SojT.thermophilus (pdb code: 2bek)
chromosome segregation
NifH / Av2A.vinelandii (pdb code: 1n2c)
electron transfer (nitrogenase turnover)
E
kDa
M 1 2 3 4 5 6 M 7 8 9 10 11
250 -
150 -
100 -
75 -
50 -
37 -
25 -
20 -
15 -
10 -
BcsE217-523
BcsQ*
BcsHisR
1: BcsHisRQWT-BcsE217-523
2: BcsHisRQR156E-BcsE217-523
3: BcsHisRQR156E-N152D-BcsE217-523
4: BcsHisRQN152D-BcsE217-523
5: BcsHisRQC39A-D41A-BcsE217-523
6: BcsHisRQD150A-BcsE217-523
7: BcsHisRQR10E-BcsE217-523
8: BcsHisRQT15K-BcsE217-523
9: BcsHisRQC39D-BcsE217-523
10: BcsHisRQR156A-N152A-N171A-BcsE217-523
11: BcsHisRQT15K-C39A-D41A-BcsE217-523
F
BcsHisRQWT
BcsHisRQC39D
BcsHisRQR156E
BcsHisRQT15K
BcsHisRQR156E-N152D
BcsRQR156E-N152D-His
A280
Elution volume, ml
#1
#2
#3
M
G
FleQT149E
BcsHisRQWT
BcsHisRQC39D
BcsHisRQR156E (#1)
BcsHisRQT15K
A620
Concentration, μM
H
ATP
ADP
BcsHisRQWT
BcsHisRQC39D
BcsHisRQR156E
BcsHisRQT15K
A254
Elution time, min
I
BcsHisRQWT-BcsE217-523
BcsHisRQR156E-BcsE217-523
FleQT149E
A280
A620
Elution volume, ml
Concentration, μM

Figure S3

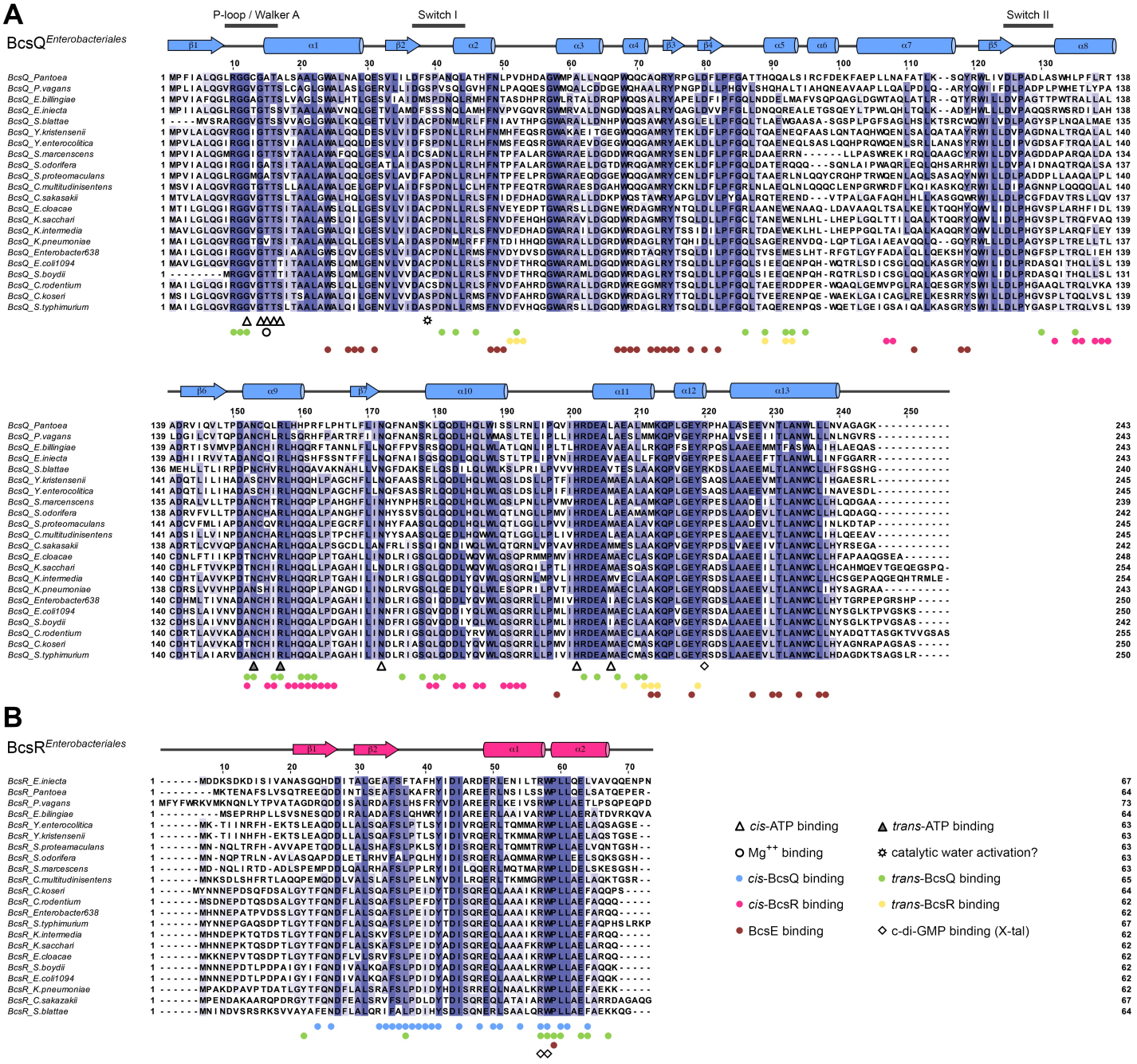
A
BcsQ Enterobacteriales
P-loop / Walker A
Switch I
Switch II
BcsQ_Pantoea
BcsQ_P.vagans
BcsQ_E.billingiae
BcsQ_E.iniecta
BcsQ_S.blattae
BcsQ_Y.kristensenii
BcsQ_Y.enterocolitica
BcsQ_S.marcenscens
BcsQ_S.odorifera
BcsQ_S.proteomaculans
BcsQ_C.multitudinisentens
BcsQ_C.sakasakii
BcsQ_E.cloacae
BcsQ_K.sacchari
BcsQ_K.intermedia
BcsQ_K.pneumoniae
BcsQ_Enterobacter638
BcsQ_E.coli1094
BcsQ_S.boydii
BcsQ_C.rodentium
BcsQ_C.koseri
BcsQ_S.typhimurium
B
BcsR Enterobacteriales
BcsR_E.iniecta
BcsR_Pantoea
BcsR_P.vagans
BcsR_E.billingiae
BcsR_Y.enterocolitica
BcsR_Y.kristensenii
BcsR_S.proteamaculans
BcsR_S.odorifera
BcsR_S.marcescens
BcsR_C.multitudinisentens
BcsR_C.koseri
BcsR_C.rodentium
BcsR_Enterobacter638
BcsR_S.typhimurium
BcsR_K.intermedia
BcsR_K.sacchari
BcsR_E.cloacae
BcsR_S.boydii
BcsR_E.coli1094
BcsR_K.pneumoniae
BcsR_C.sakazakii
BcsR_S.blattae
cis-ATP binding
trans-ATP binding
Mg++ binding
catalytic water activation?
cis-BcsQ binding
trans-BcsQ binding
cis-BcsR binding
trans-BcsR binding
BcsE binding
c-di-GMP binding (X-tal)

Figure S4

C

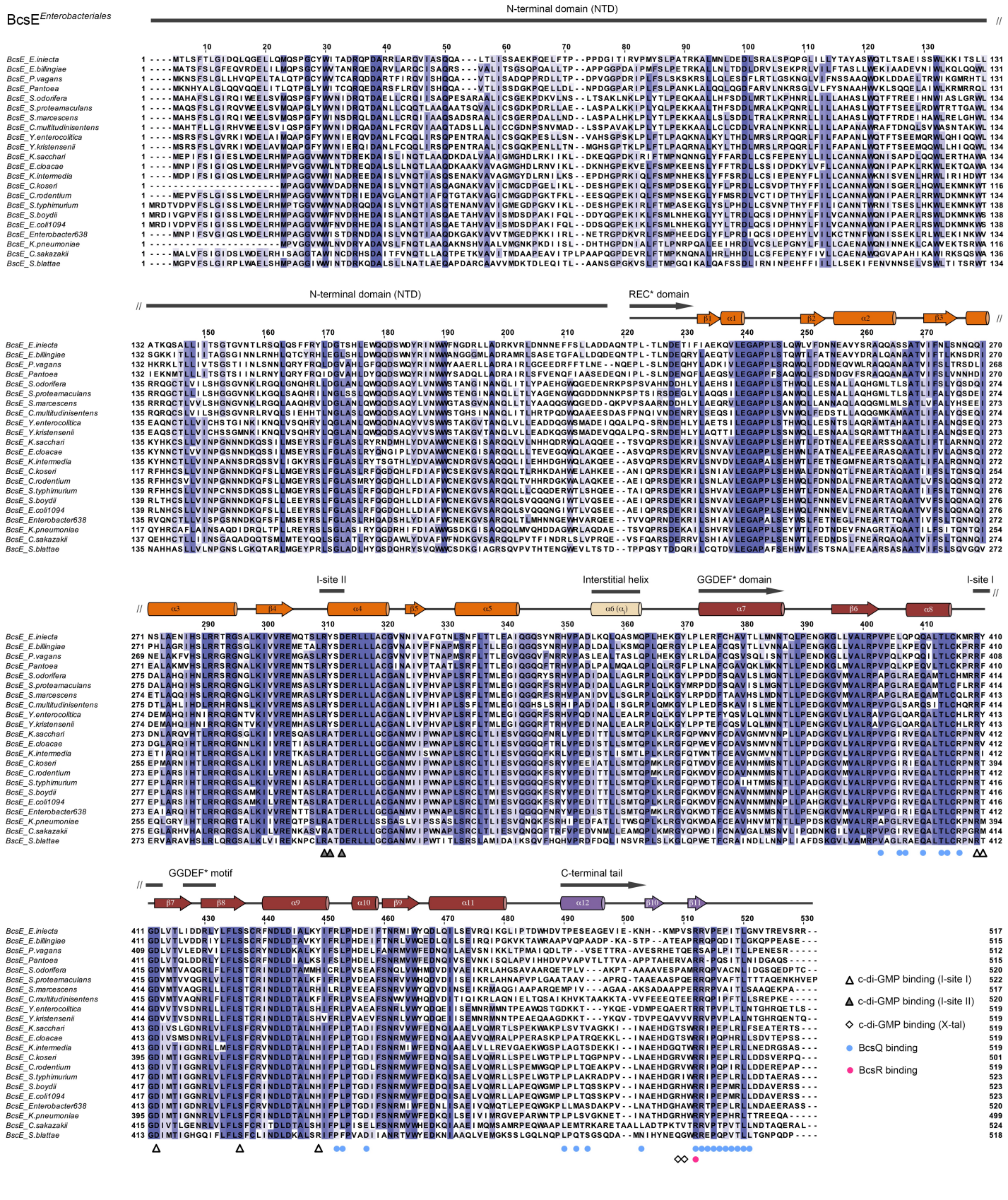
BcsE Enterobacteriales
N-terminal domain (NTD)
REC* domain
I-site II
Interstitial helix
GGDEF* domain
I-site I
GGDEF* motif
C-terminal tail
BcsE_E.iniecta
BcsE_E.billingiae
BcsE_P.vagans
BcsE_Pantoea
BcsE_S.odorifera
BcsE_S.proteamaculans
BcsE_S.marcescens
BcsE_C.multitudinisentens
BcsE_Y.enterocolitica
BcsE_Y.kristensenii
BcsE_K.sacchari
BcsE_E.cloacae
BcsE_K.intermedia
BcsE_C.koseri
BcsE_C.rodentium
BcsE_S.typhimurium
BcsE_S.boydii
BcsE_E.coli1094
BcsE_Enterobacter638
BcsE_K.pneumoniae
BcsE_C.sakazakii
BscE_S.blattae
c-di-GMP binding (I-site I)
c-di-GMP binding (I-site II)
c-di-GMP binding (X-tal)
BcsQ binding
BcsR binding

Figure S4

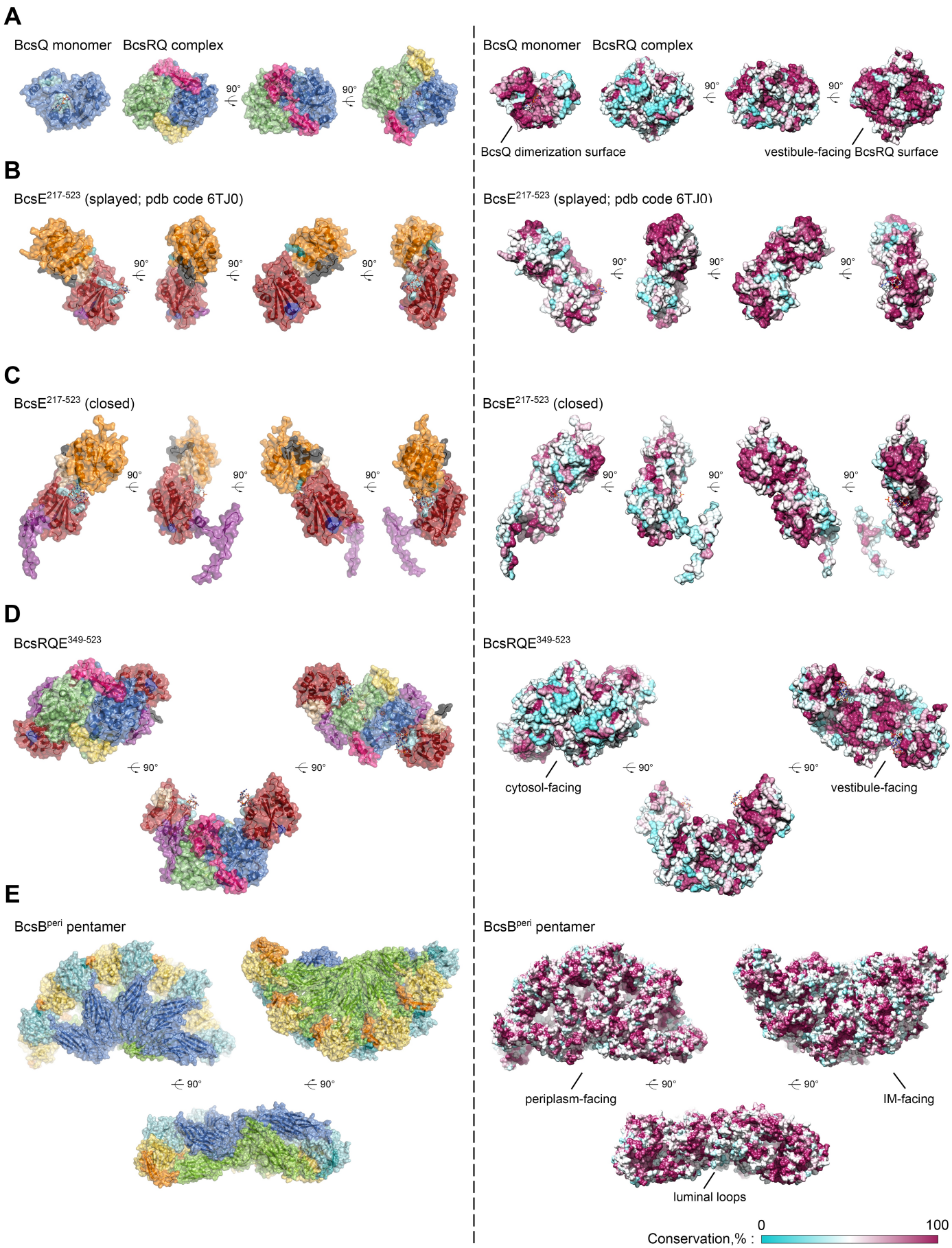
A
BcsQ monomer
BcsRQ complex
90°
90°
BcsQ monomer
BcsRQ complex
90°
90°
BcsQ dimerization surface
vestibule-facing BcsRQ surface
B
BcsE217-523 (splayed; pdb code 6TJ0)
90°
90°
90°
BcsE217-523 (splayed; pdb code 6TJ0)
90°
90°
90°
C
BcsE217-523 (closed)
90°
90°
90°
BcsE217-523 (closed)
90°
90°
90°
D
BcsRQE349-523
90°
90°
BcsRQE349-523
90°
90°
cytosol-facing
vestibule-facing
E
BcsBperi pentamer
90°
90°
BcsBperi pentamer
90°
90°
periplasm-facing
IM-facing
luminal loops
0
100
Conservation,% :

Figure S5

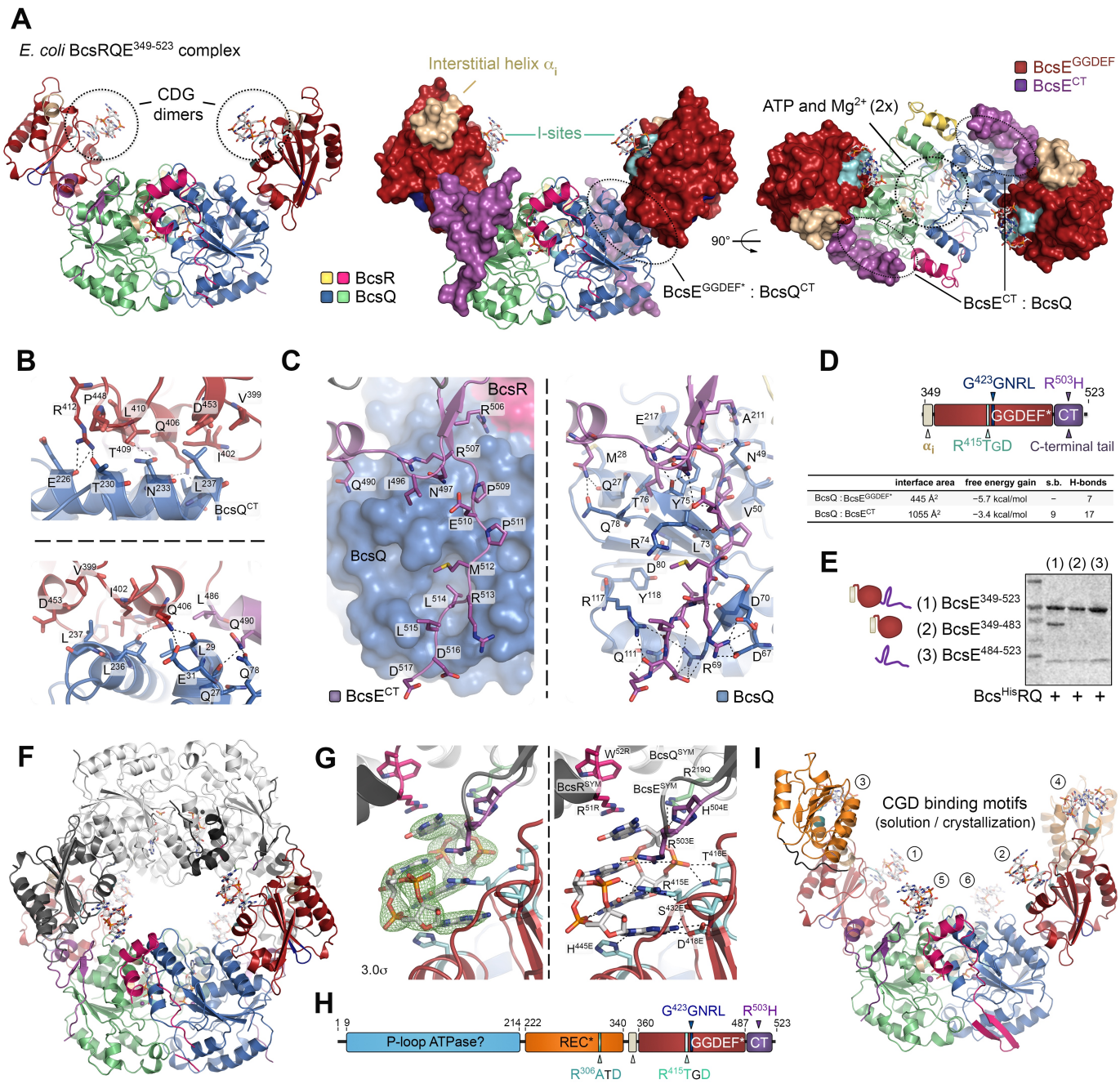
A
E. coli BcsRQE349-523 complex
CDG dimers
Interstitial helix αi
I-sites
BcsR
BcsQ
BcsEGGDEF*
BcsECT
ATP and Mg2+ (2x)
90°
BcsEGGDEF* : BcsQCT
BcsECT : BcsQ
B
BcsQCT
C
BcsR
BcsQ
BcsECT
BcsQ
D
G423GNRL R503H
349
GGDEF*
CT
523
αi
R415TGD
C-terminal tail
interface area | free energy gain | s.b. | H-bonds
BcsQ : BcsEGGDEF* | 445 Å2 | −5.7 kcal/mol | – | 7
BcsQ : BcsECT | 1055 Å2 | −3.4 kcal/mol | 9 | 17
E
(1) (2) (3)
(1) BcsE349-523
(2) BcsE349-483
(3) BcsE484-523
BcsHisRQ + + +
F
G
3.0σ
H
1 9
214 222
340 360
487
523
P-loop ATPase?
REC*
GGDEF*
CT
G423GNRL
R503H
R306ATD
R415TGD
I
CGD binding motifs
(solution / crystallization)

Figure S6

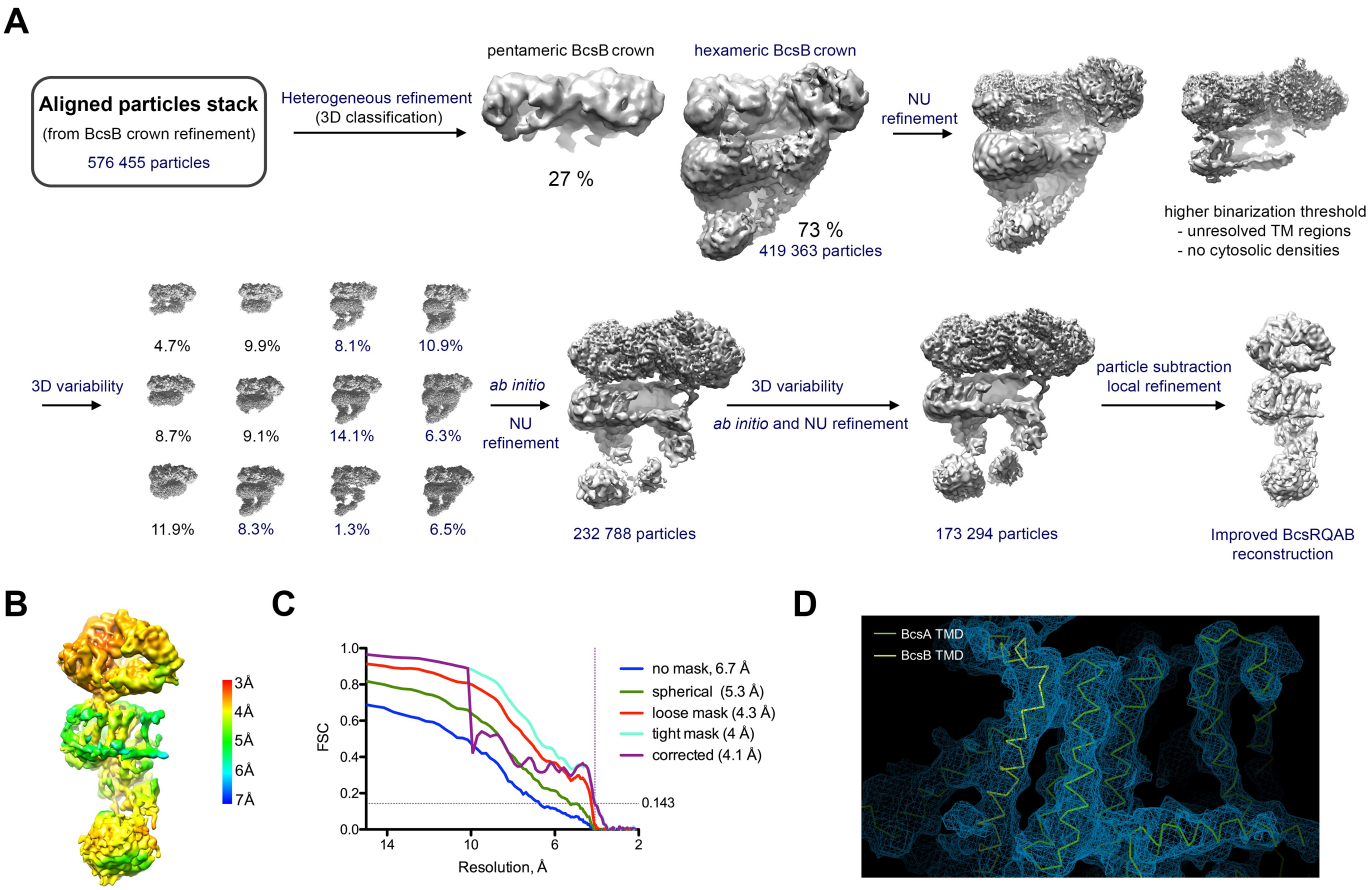
A
Aligned particles stack
(from BcsB crown refinement)
576 455 particles
Heterogeneous refinement
(3D classification)
pentameric BcsB crown
27 %
hexameric BcsB crown
73 %
419 363 particles
NU
refinement
higher binarization threshold
- unresolved TM regions
- no cytosolic densities
3D variability
4.7%
9.9%
8.1%
10.9%
8.7%
9.1%
14.1%
6.3%
11.9%
8.3%
1.3%
6.5%
ab initio
NU
refinement
232 788 particles
3D variability
ab initio and NU refinement
173 294 particles
particle subtraction
local refinement
Improved BcsRQAB
reconstruction
B
3Å
4Å
5Å
6Å
7Å
C
FSC
1.0
0.8
0.6
0.4
0.2
0.0
14
10
6
2
Resolution, Å
0.143
no mask, 6.7 Å
spherical (5.3 Å)
loose mask (4.3 Å)
tight mask (4 Å)
corrected (4.1 Å)
D
BcsA TMD
BcsB TMD

Figure S7

Table S1 | Cryo-EM data collection and refinement statistics for BcsB*	
Protein sample	Bcs macrocomplex ($Bcs^{His}RQA^{HA\text{-}FLAG}B^{Strep}EF(G)$)
Data collection	
Microscope	Titan Krios (Thermo Fisher Scientific) CM01 (ESRF)
Voltage (kV)	300
Camera	Gatan K2 Summit
Energy filter	GIF Quantum LS
Pixel size ($Å^2$)	1.05258
Collection mode	electron counting
Total electron dose ($e^-/Å^2$)	48
Movies	9 129
Frames/movie	40 (dataset I), 50 (dataset II)
Defocus range (μm)	–0.75 to –2.75
Single particles	576 455
Average map resolution	2.9 Å
Symmetry	none (C1)
Sharpening B-factor	84.4
Atomic model refinement	
* Refined macromolecular assembly	$BcsB^{peri}$ pentamer
Number of chains / residues	5 / 3132
Number of non-hydrogen atoms	
Proteins	24 330
B-factors	
Proteins (min/max/mean)	38.34/131.30/71.56
R.m.s.d.	
Bond lengths (Å)	0.005
Bond angles (deg)	0.602
Ramachandran plot	
Favored (%)	95.29
Allowed (%)	4.71
Rotamer outliers	0
Cβ outliers	0
Peptide plane (%)	
Cis proline/general	3.6 / 0
Twisted proline/general	0 / 0
CaBLAM outliers (%)	2.38
All-atom clashscore	7.02
Molprobity score	1.71

Table S2 | Crystallographic data collection and refinement statistics for the BcsRQ complex *

	$BcsRQ^{His}$	$BcsRQ^{His}$	$BcsRQ^{His}$	$BcsRQ^{His}$
Crystallized protein	SeMet	SeMet	Native	Native
Data Collection				
Space group	P 1 21 1	P 1 21 1	P 21 21 21	P 1 21 1
Cell dimensions				
a, b, c (Å)	56.1, 78.4, 65.2	57.1, 78.8, 66.6	59.1, 73.2, 140.5	57, 79, 66.8
α, β, γ (deg)	90, 97.41, 90	90, 99.28, 90	90, 90, 90	90, 99.26, 90
Wavelength	0.9793	0.9786	0.9800	0.9793
Resolution (Å)	45.2-1.89 (1.97-1.9)	46.6-2.09 (2.16-2.09)	45.2-1.59 (1.65-1.59)	46.7-1.59 (1.65-1.59)
R-merge	9.5% (116.9%)	9.5% (135%)	9.4% (192.6%)	8.5% (127%)
R-meas	10% (126.6%)	10.15% (146.7%)	9.9% (201.9%)	9.7% (156.7%)
R-pim	3.1% (47.6 %)	3.6% (56.2%)	2.7% (59.3%)	4.7% (90%)
Mean I/σ(I)	14.4 (1.2)	13.4 (1.35)	17.2 (1.05)	11.4 (0.7)
Completeness (%)	94% (69.66%)	98.7% (92.7%)	99% (91%)	95.7% (74.5%)
Multiplicity	10.1 (6.7)	7.6 (6.4)	13.2 (11.1)	3.8 (2.5)
$CC_{1/2}$	99.9 (72.7)	99.8 (68.2)	99.9 (45.9)	99.8 (41.5)
Refinement				
Unique reflections	41 607	34 175	81 658	74 521
R-work	17.8%	19.2%	16.0%	18.5%
R-free	21.8%	22.3%	18.4%	20.9%
Number of non-hydrogen atoms				
Proteins	4 328	4 367	4 592	4 596
Ligands	64	64	64	64
B-factors				
Proteins	52.07	67.37	28.93	45.65
Ligands	34.71	48.03	21.88	29.36
R.m.s.d.				
Bond lengths (Å)	0.006	0.002	0.006	0.006
Bond angles (deg)	0.79	0.51	0.78	0.81
Ramachandran plot				
Favored (%)	98.9	98.5	98.5	98.9
Allowed (%)	1.2	1.5	1.5	1.1
Molprobity score	1.01	1.02	0.94	1.08
Crystallization condition ligand	AppCp (ACP)	ADP	ADP	none
Ligand in structure	ATP / ACP **	ATP	ATP	ATP

** Statistics for the highest-resolution shell are shown in parentheses.*

*** ACP binding cannot be ruled out as the compound was present in the crystallization condition and the electron density is indistinguishable from that of ATP*

**** Ligands shown in the |Fo| - |Fc| maps calculated from models prior to inclusion of the ligands and contoured at 2σ*

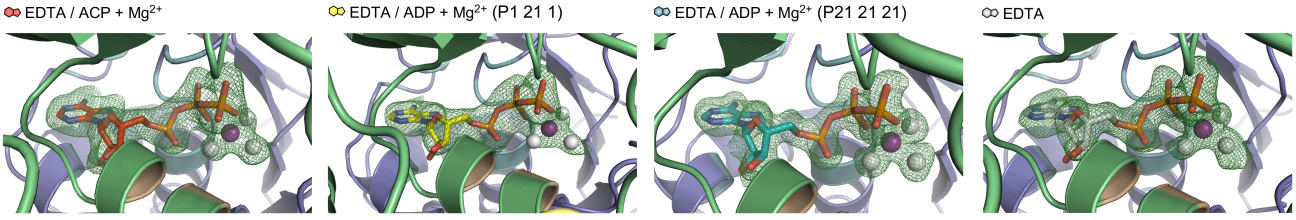

Table S3 | Crystallographic data collection and refinement statistics for BcsRQE* heterocomplexes		
	BcsRQ^{R156E}-BcsE$^{217-523}$	**BcsRQ-BcsE$^{349-523}$**
Crystallized protein	Native	Native
Data Collection		
Space group	P 21 21 21	P 1 21 1
Cell dimensions		
a, b, c (Å)	61.4, 169.6, 177.6	108, 72.6, 161.3
α, β, γ (deg)	90, 90, 90	90, 98.37, 90
Wavelength	0.9801	0.9801
Resolution (Å)	48-2.9 (3.004-2.9)	49-2.49 (2.58-2.49)
R-merge	19.18% (307%)	20.15% (156.5%)
R-meas	19.94% (319%)	21.8% (169.6%)
R-pim	5.8% (85.3%)	8.3% (64.61%)
Mean I/σ(I)	14 (0.78)	11.45 (1.1)
Completeness (%)	99.7% (99.4%)	99% (91.6%)
Multiplicity	13.6	6.9
$CC_{1/2}$	99.9 (52.5)	99.5 (46.9)
Refinement		
Unique reflections	41 967	86 089
R-work	19.96%	18.08%
R-free	22.9%	22.5%
Number of non-hydrogen atoms		
Proteins	8 851	13 823
Ligands	260	496
B-factors		
Proteins	104.58	62.38
Ligands	95.4	53.15
R.m.s.d.		
Bond lengths (Å)	0.004	0.004
Bond angles (deg)	0.68	0.7
Ramachandran plot		
Favored (%)	98.46	98.43
Allowed (%)	1.54	1.57
Molprobity score	1.24	1.09
Crystallization condition ligand	ACP, c-di-GMP	ACP, c-di-GMP
Ligand in structure **	ATP/ACP, c-di-GMP	ATP/ACP, c-di-GMP
Protein : c-di-GMP ratio	1 : 2	1 : 2

** Statistics for the highest-resolution shell are shown in parentheses*

*** ACP binding cannot be ruled out as the compound was present in the crystallization condition and the electron density is indistinguishable from that of ATP*